



SIGNAL PROCESSING IN COLD ATOM INTERFEROMETRY-BASED INS

THESIS

Kara M. Willis, Civilian, DAF

AFIT-ENG-14-M-84

**DEPARTMENT OF THE AIR FORCE
AIR UNIVERSITY**

AIR FORCE INSTITUTE OF TECHNOLOGY

Wright-Patterson Air Force Base, Ohio

**DISTRIBUTION STATEMENT A:
APPROVED FOR PUBLIC RELEASE; DISTRIBUTION UNLIMITED**

The views expressed in this thesis are those of the author and do not reflect the official policy or position of the United States Air Force, the Department of Defense, or the United States Government.

This material is declared a work of the U.S. Government and is not subject to copyright protection in the United States.

AFIT-ENG-14-M-84

SIGNAL PROCESSING IN COLD ATOM INTERFEROMETRY-BASED INS

THESIS

Presented to the Faculty
Department of Electrical and Computer Engineering
Graduate School of Engineering and Management
Air Force Institute of Technology
Air University
Air Education and Training Command
in Partial Fulfillment of the Requirements for the
Degree of Master of Science in Electrical Engineering

Kara M. Willis, BS
Civilian, DAF

March 2014

DISTRIBUTION STATEMENT A:
APPROVED FOR PUBLIC RELEASE; DISTRIBUTION UNLIMITED

AFIT-ENG-14-M-84

SIGNAL PROCESSING IN COLD ATOM INTERFEROMETRY-BASED INS

Kara M. Willis, BS
Civilian, DAF

Approved:

//signed//
Meir Pachter, PhD (Chairman)

13 March 2014
Date

//signed//
Maj Marshall Haker, PhD (Member)

10 March 2014
Date

//signed//
Kyle Kauffman, PhD (Member)

10 March 2014
Date

Abstract

High precision Cold Atom Interferometers (CAI) are in development to supplement or replace conventional, navigation quality inertial measurement units. A major drawback of the atomic interferometers is their low duty cycle and sampling rate, caused by delays required for cooling the atoms and collecting acceleration and angular rate measurements. A method is herein developed for inertial navigation by integrating highly accurate, low duty cycle CAI measurements with high bandwidth, conventional Inertial Navigation System (INS) measurements. A fixed-lag smoothing algorithm is used to estimate optimal acceleration and angular rate measurements from the CAI and INS data. Given current CAI limitations, simulation results demonstrate nearly 50 percent error reduction for the enhanced INS compared to a conventional, unaided INS. When the conventional INS position error was increased by 500 (m/hr), the 50 percent error reduction from aiding was maintained. Increasing the conventional INS data rate fifteen-fold while maintaining a 1 Hz CAI sample rate leads to an approximately 6 percent increase in navigation error, suggesting that the CAI-aiding algorithm effectivity is only slightly influenced by the conventional INS data rates. A five-fold increase of the CAI measurement rate shows approximately 80 percent reduction in navigation error, supporting the potential for significant performance gains in the near future from advancements in cold atom technology.

Acknowledgments

I would like to express gratitude to my faculty advisor, Dr. Meir Pachter, for his consistent guidance and support over the course of this thesis effort. I would also like to thank my subject matter mentors, Maj Marshall Haker and Dr Kyle Kauffman, for their insights and unwavering encouragement.

Kara M. Willis

Table of Contents

	Page
Abstract	iv
Acknowledgments	v
Table of Contents	vi
List of Figures	viii
List of Tables	ix
 I. Introduction	 1
1.1 Research Motivation	1
1.1.1 Inertial Navigation	2
1.1.2 Cold Atom Interferometry	3
1.2 Problem Definition	6
1.3 Related Research	6
1.3.1 Multiple INS Integration	6
1.3.2 CAI Integration with Conventional INS	7
1.4 Scope and Assumptions	8
1.5 Methodology	9
 II. Mathematical Background	 10
2.1 Notation	10
2.2 Reference Frames	10
2.2.1 True Inertial Frame	11
2.2.2 Earth-Centered Inertial Frame (i-frame)	11
2.2.3 Earth-Centered Earth-Fixed Frame (e-frame)	11
2.2.4 Navigation Frame (n-frame)	11
2.2.5 Body Frame (b-frame)	11
2.3 Inertial Navigation	12
2.3.1 Mechanization Equations	12
2.3.2 Strapdown Error States	13
2.4 Kalman Filter	15
2.4.1 State Model	16
2.4.2 Measurement Model	17
2.4.3 Kalman Filter Algorithm	18

	Page
III. Algorithm Development and Model Creation	22
3.1 Postulate	22
3.2 Signal Processing	24
3.3 Proof of Concept	32
3.4 Navigation	33
3.5 Simulation	38
3.6 Revision of Model 1	39
3.7 Alternate Model	40
IV. Results and Analysis	44
4.1 Monte Carlo Analysis	44
4.1.1 Varying Conventional INS Data Rate	45
4.1.2 Varying Acceleration Input	48
4.1.3 Varying CAI Measurement Data Rate	50
V. Conclusions and Recommendations	52
5.1 Conclusion	52
5.2 Recommendations for Future Research	52
Appendix A: Analytic Sensor Drift Modeling	54
A.1 Gyro Drift	54
A.2 Accelerometer Drift	56
Appendix B: Calibration for Bias and Drift Uncertainty	60
Bibliography	62

List of Figures

Figure	Page
1.1 Atom Chip [6]	2
1.2 Comparison of Optical and Atom Interferometer (Mach-Zehnder type configuration).	5
2.1 Visualization of Local Level Plane with associated body frame and navigation frame.	13
2.2 Kalman Filter Process [15]	20
2.3 Residual Monitoring and Sensor Failure Detection [14]	21
3.1 Model 1: Acceleration over one duty cycle (k)	23
3.2 Revised Model 1. Acceleration over two CAI duty cycles.	40
3.3 Model 2 System Concept.	41
4.1 Monte Carlo Simulation results for Position Error over 1000 runs. Calibrated standard deviation position error for conventional INS is 1000 (m/hr).	45
4.2 Monte Carlo Simulation results for Position Error over 1000 runs. Calibrated standard deviation position error for conventional INS was 1500 (m/hr)	46
4.3 Position Error Corrections from Monte Carlo Simulations for Varying Conventional INS Data Rates.	48

List of Tables

Table	Page
4.1 Sensor Uncertainties for Scenario 1 = 1000 (m/hr), Scenario 2 = 1500 (m/hr) .	44
4.2 Unaided, Aided Error and Error Correction Values after One Hour for Varied INS Drifts	47
4.3 Calibrated Conventional INS Uncertainties for Different Data Rates	47
4.4 Unaided and Aided RMS Error after One Hour for Varied INS Data Rates . . .	49
4.5 Unaided, Aided Error and Error Correction Values after One Hour for Varied Acceleration	50
4.6 Unaided, Aided Error and Error Correction Values after One Hour for Varied CAI Data Rates	51

SIGNAL PROCESSING IN COLD ATOM INTERFEROMETRY-BASED INS

I. Introduction

1.1 Research Motivation

Precision navigation is critical for numerous applications in both civilian and defense sectors, from vehicle guidance to accurate target location. Historically, passive inertial navigation was the dominant guidance system used for naval and aviation purposes, but lost favor after the widespread introduction of the Global Positioning System (GPS). Recent advances in GPS technology now provide centimeter-level measurements for users in certain applications. Users have developed a dependency upon GPS, a weakness which our enemies exploit by interfering with its signals, often via low cost methods. In addition to deliberate threats, GPS has a number of other limitations. Sub-meter GPS accuracy is only attainable when users' receivers have uninterrupted tracking of at least four GPS satellites [1]. Large buildings, canyons and indoor environments still pose problems for users attempting to acquire and track GPS signals. In light of these limitations and the recognized dependency, interest has reverted toward alternative, passive sensors for aiding Inertial Navigation Systems (INSs), particularly for military operations. This research will investigate the feasibility of using a Cold Atom Interferometer (CAI) as a passive navigation aid.

Demonstrations in cold atom interferometry technology show the potential for collecting high precision measurements in the fields of navigation, gradiometry, geophysics and atomic clocks [2]. Numerous universities are researching hardware designs and improvements for cold atom interferometers, including Stanford and Ben-Gurion University in Israel [3], [4]. Stanford University has demonstrated the performance of a

large, 1 (m³) prototype CAI used for ground navigation, as well as a compact CAI for collecting aerial gradiometry measurements. The CAI performance characteristics used in this thesis are referenced from the Stanford University demonstrations [5]. Ben-Gurion University has recently developed a CAI fabricated chip, illustrated in Figure 1.1, which opens the possibilities for compact, affordable applications in the near future [4].

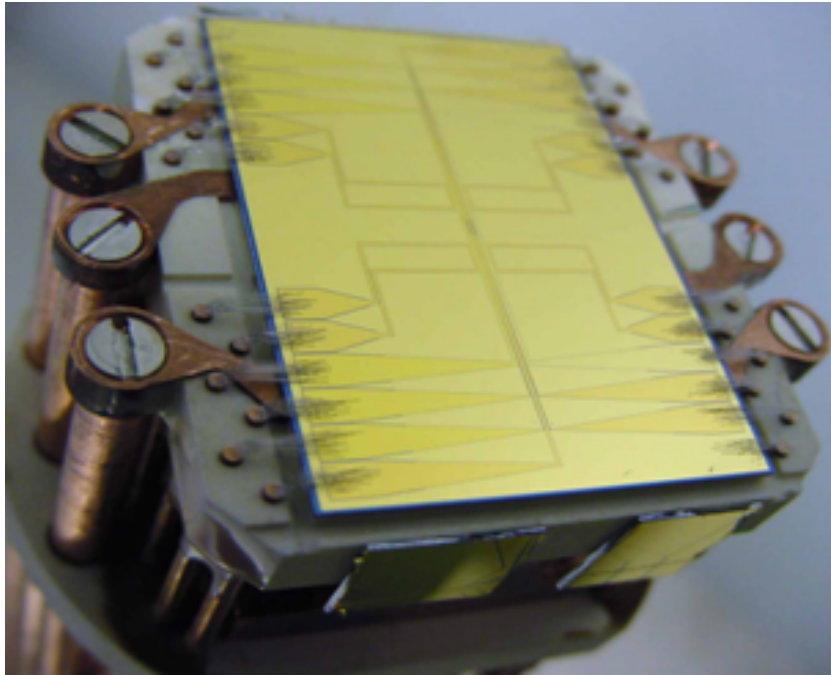


Figure 1.1: Atom Chip [6]

1.1.1 Inertial Navigation.

Inertial navigation is the process of measuring position, velocity and orientation through use of dead-reckoning inertial sensors. Specifically, inertial navigation systems use acceleration and angular rotation rate measurements collected from accelerometers and gyroscopes (gyros), and then integrate these measurements to determine position, velocity and attitude [7]. The measured acceleration is the sum of linear acceleration and

gravity along the accelerometer's input axis of measurement. Integration of the gyroscopes' rotation rates provides angular orientation so that the acceleration vector may be resolved in a reference frame. Typical strapdown inertial navigation systems are thus composed of three accelerometers and three gyroscopes to collect measurements from the three orthogonal axes. The strapdown INS is a digital alternative to the mechanical gimbal and is used predominately in aerospace navigation because of its improved reliability, lighter weight, and reduced costs. Ring laser or fiber optic interferometers act as rate gyroscopes and accelerometers in the strap down systems and can collect measurements on the order of 300 Hz. The INS is also a passive system, which makes its operation impervious to external denial techniques and makes them very useful for military applications against jamming or spoofing threats [7]. Despite the passive nature and high sampling rates, small sensor errors, which are integrated as part of the inertial measurements, cause the INS accuracy to degrade and become unreliable over time. Thus, the INS measurements require aiding from other sensors, typically GPS, to bound error growth [7].

1.1.2 Cold Atom Interferometry.

Conceptually, the cold atom interferometer design is similar to an optical interferometer used in both ring laser and fiber optic gyros. Using reflectors and beam splitters, a ring laser interferometer guides counter-propagating light beams and then collects rotation information from the resultant interference patterns as illustrated in Figure 1.2. Similarly, atomic 'matter' waves are split using either material structures or light fields [8] as shown by the π and $\frac{\pi}{2}$ beams shown in Figure 1.2. The atom waves are then guided using either lasers or magnetic fields [4]. The wavelength of the atomic wave, λ , is related to the momentum p of the atom according to the quantum mechanics relationship as follows [8]:

$$\lambda = \frac{h}{p} = \frac{h}{mv} \quad (1.1)$$

where h is Plank's constant, m is the atom's mass and v is its velocity. In general, CAI physics is based upon de Broglie's wave-particle duality hypothesis which states that at

the quantum level, matter exhibits wave-like properties [5]. In the CAI, cooled atoms are guided through a vacuum and their resultant acceleration-induced phase shifts are measured via a diffraction grating. The phase shift $\Delta\phi_{light}$ is analogous to the Sagnac effect in the optical interferometers and can be described by [5]

$$\Delta\phi_{light} = \frac{4\pi\Omega A}{\lambda c} \quad (1.2)$$

where Ω is the angular rate of the instrument, c is the speed of light, and A is the enclosed area of the interferometer's optical path. The phase shifts cause interference patterns on the diffraction grating from which phase information is collected and used to determine angular rotation. Additionally, because of their particle nature, the atoms may be treated as inertial masses and their movement is used to determine the CAI system's acceleration.

Despite functional similarities, the CAI's atom wave interferometer offers the advantage of higher sensitivity to inertial forces as compared to the conventional, optical interferometer in strapdown INS. The group velocity of the atoms is relatively small compared to the speed of light, so very small accelerations will still induce a significant change in the atom beam's path, causing measureable phase shifts in the interference signal. If A is held constant, theoretically CAI is more sensitive to rotation than an optical interferometer by a factor of 10 since atomic mass is greater than the light photon's relative mass [3]. This is expressed in the following equation, where $\delta\phi_{light}$ was defined in (1.2), and $\delta\phi_{atom}$ is the atom phase shift:

$$\frac{\delta\phi_{atom}}{\delta\phi_{light}} = \frac{m}{h/(\lambda c)} > 10^{10}$$

Evaporative cooling techniques allow for precise control of the velocity and position of the atoms in the atomic wave. The low temperatures necessary to cool the atoms also improve the CAI's signal-to-noise ratio and its sensitivity to external fields [8].

However, there are some factors which reduce the CAI sensitivity, including bandwidth and duty cycle. Due to low bandwidth associated with high precision sensors,

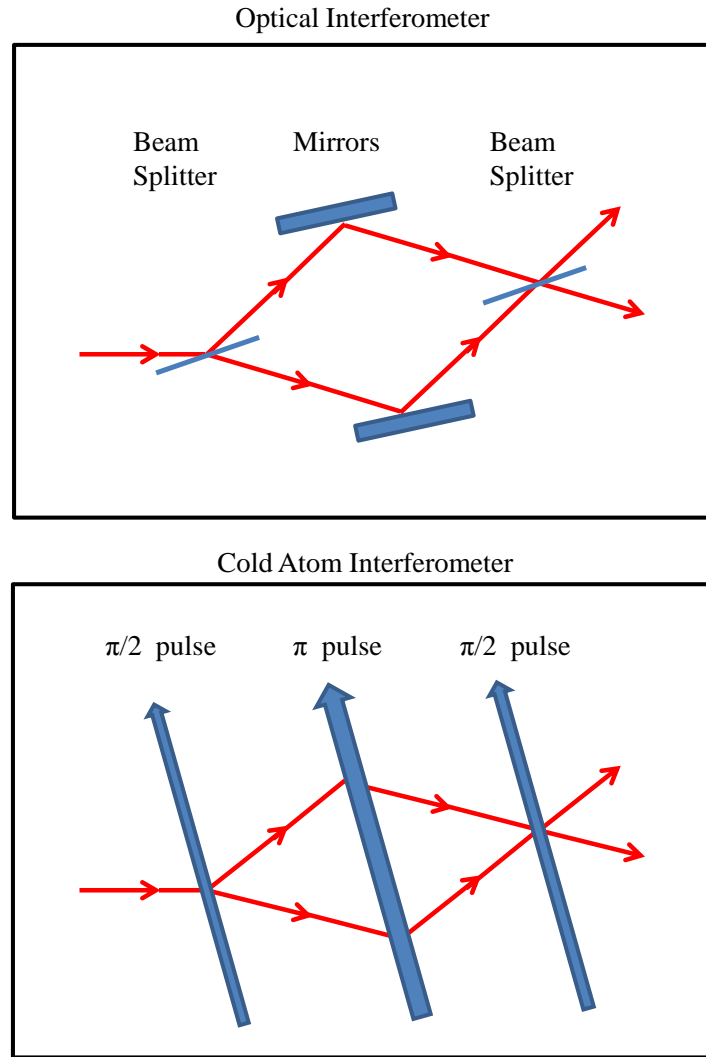


Figure 1.2: Comparison of Optical and Atom Interferometer (Mach-Zehnder type configuration).

large dynamics may cause the path of the atom particles to exceed the sensor's detection threshold. Thus, a high dynamic environment may produce unreliable measurements or CAI system failure. Additionally, the time duration for collecting a CAI measurement is on the order of 1 Hz [8], which leads to a loss in collected information as compared to the

typical 50-300 Hz sample availability provided by conventional strap-down INS. The main themes for this research are both understanding and compensating for this latter issue.

1.2 Problem Definition

The objective of this thesis is to explore Inertial Navigation using CAI-based acceleration and angular rate measurements. While CAI-based measurements are very accurate, the rate at which they can be obtained is relatively low, e.g. 1 Hz. The low duty cycle is caused by delays required for cooling the atoms and collecting acceleration and angular rate measurements [5], [8]. Less accurate, conventional INS measurements, which are available at a much higher rate, might be used to fill the temporal gap in CAI measurements. In addition, the CAI measurements represent an average of the true acceleration and angular rate during the collection phase of the duty cycle. Therefore, the CAI measurement may be combined with the conventional INS data during this phase to reduce the overall navigation error. For a CAI sensor with 50 percent duty cycle, the conventional INS measurements would be used for navigation during the first half of the duty cycle where CAI measurements are unavailable. Subsequently, a weighted combination of 1) the conventional INS-provided multiple measurements, and 2) the single, CAI-based acceleration and angular rate measurements would be used for the second half of the duty cycle.

1.3 Related Research

1.3.1 Multiple INS Integration.

Omr, Georgy and Noreldin propose a method for integrating the accelerometer measurements from multiple MEM sensors for pedestrians in [9]. The authors show that Micro Electro-Mechanical System (MEMS) measurements from multiple devices carried on different parts of the user may be collected and combined wirelessly. Associated covariances for the position and velocity measurements are used to calculate the best

estimate for a unified navigation solution, or conversely, used to update all the individual MEM's measurement solutions. The covariance weighting algorithm requires less computing power than a centralized Kalman filter because it only updates the solutions. In other words, propagation of an internal Kalman filter model is unnecessary. This method allows for integrating an unrestricted number of inertial navigation sensors, which the authors note is a challenge in centralized Kalman filters.

This thesis differs from Omr's research in that this work considers more complex inertial navigation sensors, corresponding measurements, and purpose. The cold atom interferometer and INS sensor are much more accurate than MEMs and provide angular rate measurements in addition to acceleration measurements. Thus, while Omr's research is limited to aiding position and velocity, this thesis also proposes methods for aiding attitude. Additionally, this thesis accounts for the problems posed by integrating measurements from sources which operate at different sample rates and duty cycles. Finally, while Omr et al focus on pedestrian navigation, this thesis applies multiple sensor integration to three dimensional aircraft navigation.

1.3.2 CAI Integration with Conventional INS.

Jekeli [5] proposes a model for the cold atom interferometer which, with some reasonable assumptions, can be viewed as analogous to the conventional INS. Using bias and drift parameters associated with the accelerometers and gyroscope, he demonstrates the CAI inertial sensor's theoretical performance. The acceleration and gyroscope measurement models presented in Jekeli's research [5], and substantiated in [10], are used for the CAI and conventional INS measurements in this thesis.

Canciani and Raquet propose three filter frameworks to integrate a CAI with a conventional, navigation-grade INS [11]. The first framework corrects the INS acceleration and attitude measurements and when available, mechanizes off the CAI measurements. The second framework always uses the conventional INS in the mechanization equations,

but uses the CAI delta-velocities and delta-thetas to correct the navigation solution at the position level. The third framework proposes integrating CAI with GPS measurements in order to compensate for GPS outages. When outage times were very short, the first framework showed the best results, while the second framework showed the best results during the longer, high-g CAI outages. The simulation tests assumed that the CAI measurements would be available consistently until outages occurred; for example, a duty cycle of 80 percent was modeled as a square wave with periodic 2 minute outages.

While Canciani's research focused on the CAI dropouts and outages, this thesis investigates the effects from the CAI's low duty cycle, sampling rates, and the analysis methods to compensate for them. This thesis makes measurement corrections on the acceleration and angular rate level, similar to the first framework. However, Kalman filter modeling is not used; rather, this thesis implements an estimation algorithm similar to a fixed-lag smoother.

1.4 Scope and Assumptions

This research uses a proof of concept approach to model the CAI and INS errors and performance characteristics. The acceleration and gyroscope error models are composed of a bias and discrete measurement drift based upon a continuous-time, stochastic process. The analytical development of the latter is made in Appendix A. A linear relationship is assumed between the sensor's drift induced measurement variances and bias variances, which allows for calibration using the Lyapunov covariance equation in Appendix B. Furthermore, the Earth model is simplified to a flat, non-rotational environment to simplify the mechanization equations. This assumption neglects the effects of Coriolis acceleration, Schuler cycle, transport rate and other frame translational errors introduced from the Earth's curvature and rotation. Altitude aiding from barometric data or radar altimeter measurements is neglected, although it would be generally present in conventional, navigation-grade INS.

As noted earlier, this research focuses on the limitations of CAI aiding pertaining to the low duty cycle and data rate. Additional effects from high dynamic dropouts are neglected, although it is assumed that an integrity monitor would exist in a fielded implementation to disregard CAI data when dynamics exceeded an experimentally determined g-level.

1.5 Methodology

In order to integrate the CAI with the INS, measurement models were developed and error parameters were calibrated to meet their respective theoretical performances. These error parameters were used to create stochastic random variables which corrupted a simulated truth. The availability of the CAI and conventional INS measurement samples was modeled. An analytical method was developed based upon this model to combine the measurement samples and estimate their bias and drift variances for each periodic CAI duty cycle. MATLAB software was used to simulate noisy conventional INS and CAI measurements and then integrate them according to the proposed algorithm methods. The resultant error means and standard deviations were tabulated a part of a Monte Carlo analysis.

Chapter 2 presents the mathematical background necessary to understand basic inertial navigation, error modeling, and basic Kalman Filtering. Chapter 3 develops the aforementioned measurement models and the proposed algorithms for integrating them. Chapter 4 presents the methods used to statistically analyze the simulation results. Error characterizations were made by evaluating the statistical results of multiple, hour-long runs to nullify the effects of potential anomalous behavior in single runs. Chapter 5 presents a conclusion of the data analysis, CAI aiding performance, and recommendations for improvements. Areas of future research are also suggested based upon predicted technological developments.

II. Mathematical Background

This chapter presents the background information required to understand the navigation topics and mathematics discussed in the presented research. It covers basic notation, reference frames, inertial navigation system models and an overview of Kalman filters.

2.1 Notation

Notation used consistently is described below:

Scalars: denoted as upper or lower case italic letters.

Vectors: denoted as lower case bold font letters and assumed as column vectors unless otherwise specified.

Matrices: denoted as upper case bold font letters and may have subscripts specifying rows and columns.

Transpose: denoted by a superscript T.

Estimated variables: denoted by the *hat* superscript (e.g. \hat{x}).

Reference frame: denoted by superscript in parentheses (e.g. $x^{(a)}$ is a scalar in the 'a' frame).

2.2 Reference Frames

A reference frame is necessary for expressing and measuring the motion of bodies in navigation. Depending upon the scope, some reference frames are more convenient than others. All reference frames discussed herein use three-dimensional axes, with right hand, orthonormal basis.

2.2.1 True Inertial Frame.

A true inertial frame is a theoretical, non-accelerating frame from which Newton based his first law of motion. Due to relativity, this frame has no origin and is stationary relative to absolute time.

2.2.2 Earth-Centered Inertial Frame (i-frame).

The Earth-centered inertial frame is defined by the fixed stars, with an origin at the center of the earth. The vertical axis aligns with the North Pole and horizontal x-axis and y-axis lie along the equatorial plane. This frame is non-rotating, but does follow the Earth's rotation about the sun. However, because the Earth's orbit about the sun is very slow in relation to navigation about the earth, the i-frame may be approximated as a true inertial frame.

2.2.3 Earth-Centered Earth-Fixed Frame (e-frame).

As its name implies, the Earth-Centered Earth-Fixed (ECEF) frame also has an origin at the center of the earth. However, its horizontal axes *move* to coincide with the earth's rotation. The x-axis points to the Greenwich Meridian and the y-axis points to 90 degrees east longitude [7].

2.2.4 Navigation Frame (n-frame).

The navigation frame origin coincides with the location of the navigation system of interest. The vertical axis points downward in the direction of the local vertical—defined as the gravity vector for a given location on the Earth. The x-axis and y-axis point North and East, respectively, giving rise to the familiar North-East-Down (NED) convention. The navigation system's motion causes the navigation frame to rotate at the transport rate ω_{en} .

2.2.5 Body Frame (b-frame).

The body frame origin is co-located with the n-frame, but rigidly attached to the vehicle. That is, the x, y, and vertical z axes point in the direction of the aircraft nose, right wing and bottom of the aircraft, respectively. The axis set rotates with roll, pitch,

and yaw angles as the aircraft moves. It is important to note that in strapdown INS, the accelerometer and gyroscope measurements are initially resolved in the b-frame and then converted to the navigation frame using the Euler angles via Direction Cosine Matrices (DCM).

2.3 Inertial Navigation

2.3.1 Mechanization Equations.

The following equations are derived from [11] and [7]. For this research, the reference frame for the systems of interests will be the local geographical level, i.e. navigation frame. The inertial navigation system accelerometers measure the specific force vector \mathbf{f} , which is the difference between the inertial accelerations, $\ddot{\mathbf{r}}^{(i)}$, and gravity $\mathbf{g}^{(i)}$:

$$\mathbf{f}^{(i)} = \ddot{\mathbf{r}}^{(i)} - \mathbf{g}^{(i)}$$

Rearranging, the acceleration in the navigation frame with respect to the earth is:

$$\dot{\mathbf{v}}_e^{(n)} = \mathbf{f}^{(n)} - (2\boldsymbol{\omega}_{ie}^{(n)} + \boldsymbol{\omega}_{en}^{(n)}) - \mathbf{g}^{(n)} \quad (2.1)$$

where $\mathbf{g}^{(n)}$ is gravity in the navigation frame, $\mathbf{f}^{(n)}$ is specific force in the navigation frame, $\boldsymbol{\omega}_{ie}^{(n)}$ is the rotational rate of the Earth, $\boldsymbol{\omega}_{en}^{(n)}$ is the transport rate, and the term $(2\boldsymbol{\omega}_{ie}^{(n)} + \boldsymbol{\omega}_{en}^{(n)})$ is the Coriolis acceleration caused from navigating in a non-inertial, rotating reference frame [12]. Integrating (2.1) gives the three dimensional velocity vector

$$\dot{\mathbf{x}}_e^{(n)} = \mathbf{v}_e^{(n)} \quad (2.2)$$

To simplify analysis, this research assumed a nonrotating and flat Earth, which ignores the effects of the Coriolis acceleration, so that the n-frame \equiv i-frame. The inertial system accelerometers only provide measurements in the body frame, so a DCM, $\mathbf{C}_b^{(n)}$ is used to resolve the force vector into the navigation frame

$$\dot{\mathbf{C}}_b^{(n)} = \mathbf{C}_b^{(n)} \boldsymbol{\Omega}_{nb}^{(b)}$$

In our simplified inertial frame, the DCM becomes simply the identity matrix and $\omega_{nb}^{(b)}$ is assumed equivalent to $\omega_{ib}^{(b)}$.

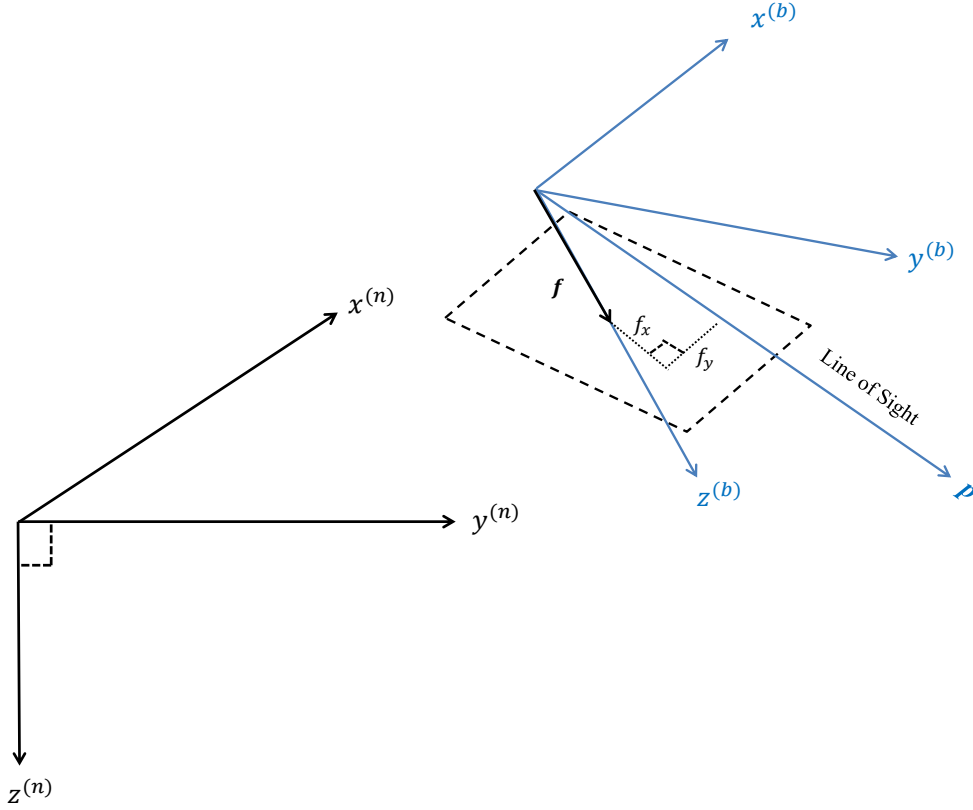


Figure 2.1: Visualization of Local Level Plane with associated body frame and navigation frame.

2.3.2 Strapdown Error States.

Since a non-rotating, flat Earth is assumed, flight in the local level plane may be visualized as Figure 2.1 where the specific force vector \mathbf{f} is comprised of the axis specific

components f_{x_i} , f_{y_i} , and f_{z_i} of the i-frame [13]

$$\begin{aligned} f_{x_i} &= f_{x_b} \cos\theta + f_{z_b} \sin\theta \\ f_{y_i} &= 0 \\ f_{z_i} &= -f_{x_b} \sin\theta + f_{z_b} \cos\theta \end{aligned} \quad (2.3)$$

where θ is the aircraft pitch angle and f_{x_b} and f_{z_b} are the axis specific force components in the b-frame. Perturbing (2.3) gives the specific force error equations

$$\begin{aligned} \delta f_{x_i} &= (-f_{x_b} \sin\theta + f_{z_b} \cos\theta) \delta\theta + \delta f_{x_b} \cos\theta + \delta f_{z_b} \sin\theta \\ &= f_{z_i} \delta\theta + \delta f_{x_b} \cos\theta \delta f_{z_b} \sin\theta \\ \delta f_{y_i} &= 0 \\ \delta f_{z_i} &= -(f_{x_b} \cos\theta + f_{z_b} \sin\theta) \delta\theta - \delta f_{x_b} \sin\theta + \delta f_{z_b} \cos\theta \\ &= -f_{x_i} \delta\theta - \delta f_{x_b} \sin\theta \delta f_{z_b} \cos\theta \end{aligned}$$

The errors in acceleration, velocity, and angular rate are found by perturbing equations (2.1) and (2.2):

$$\begin{aligned} \delta \dot{x}_i &= \delta v_{x_i} \\ \delta \dot{y}_i &= 0 \\ \delta \dot{z}_i &= \delta v_{z_i} \\ \delta \dot{v}_{x_i} &= \delta f_{x_i} = f_{z_i} \delta\theta + \cos\theta \delta f_{x_b} + \sin\theta \delta f_{z_b} \\ \delta \dot{v}_{y_i} &= 0 \\ \delta \dot{v}_{z_i} &= \delta f_{z_i} = -f_{x_i} \delta\theta - \sin\theta \delta f_{x_b} + \cos\theta \delta f_{z_b} \\ \delta \dot{\theta} &= \delta \omega \end{aligned} \quad (2.4)$$

where $\delta \dot{x}_i$, $\delta \dot{y}_i$, and $\delta \dot{z}_i$ are the axis specific velocity errors; $\delta \dot{v}_{x_i}$, $\delta \dot{v}_{y_i}$, and $\delta \dot{v}_{z_i}$ are the axis specific acceleration errors; and $\delta \dot{\theta}$ is the angular rate error.

If we further assume wings level, constant altitude flight, then the vertical force f_{z_i} simplifies to the gravitational acceleration, g ; the horizontal force δf_{x_i} simplifies to the horizontal acceleration, a , and $\theta = 0$. The equations from (2.4) are combined to form a 9×9 error state vector $\delta \mathbf{x}$ as follows:

$$\delta \mathbf{x} = \begin{bmatrix} \delta \mathbf{p} & \delta \mathbf{v} & \delta \boldsymbol{\Psi} \end{bmatrix}^T$$

where $\delta \mathbf{p}$, $\delta \mathbf{v}$ are the position and velocity errors vectors, and $\delta \boldsymbol{\Psi}$ is a 3×1 vector of angular errors due to misalignment from the navigation frame, that is

$$\begin{aligned} \delta \boldsymbol{\Psi} &= -\delta \mathbf{C}_b^{(n)} \cdot \mathbf{C}_n^{(b)} \\ &= -\delta \mathbf{C}_b^{(n)} \\ &= \begin{bmatrix} -\delta \psi & -\delta \theta & -\delta \phi \end{bmatrix}^T \end{aligned}$$

The navigation state error $\delta \dot{\mathbf{x}}$ equation (with driving inputs $\delta \mathbf{f}^{(b)}$ and $\delta \boldsymbol{\omega}_{nb}^{(b)}$) is

$$\delta \dot{\mathbf{x}} = \mathbf{M} \delta \mathbf{x} + \boldsymbol{\Gamma} \begin{bmatrix} \delta \mathbf{f}^{(b)} \\ \delta \boldsymbol{\omega}_{nb}^{(b)} \end{bmatrix}$$

where

$$\mathbf{M} = \begin{bmatrix} \mathbf{0} & \mathbf{I} & \mathbf{0} \\ \mathbf{0} & \mathbf{0} & \mathbf{F}^{(n)} \\ \mathbf{0} & \mathbf{0} & \mathbf{0} \end{bmatrix}, \quad \boldsymbol{\Gamma} = \begin{bmatrix} \mathbf{0} & \mathbf{0} \\ \mathbf{C}_b^{(n)} & \mathbf{0} \\ \mathbf{0} & -\mathbf{C}_b^{(n)} \end{bmatrix}$$

In wings level flight, $\mathbf{F}^{(n)}$ is the skew symmetric form of the specific force vector $\mathbf{f}^{(n)}$:

$$\mathbf{F}^{(n)} = \begin{bmatrix} 0 & g & 0 \\ -g & 0 & -a \\ 0 & a & 0 \end{bmatrix}$$

2.4 Kalman Filter

The Kalman filter is a linear, recursive, optimal data processing algorithm used to estimate the unknown states of a stochastic differential equation. Using current, noisy

measurements of some components of the state, and a state estimate based on the previous measurements, the Kalman filter calculates the current, statistically optimal states. The predicted current state is more accurate than the measured state, which is affected by sensor noise. Unlike batch estimation techniques, storing a history of measurements or estimates is unnecessary because the statistical information is contained within the Kalman filter's recursive state estimates and associated covariance. The Kalman filtering algorithm is based upon the following key assumptions: the linear mathematical model is an accurate representation of the true system, all the random process errors in the model and measurements are white Gaussian noises and the measurement observations are uncorrelated [14], [15]. It should be noted that no true process is perfectly described by a linear model, thus filter tuning and modification are sometimes necessary to achieve the best solution.

2.4.1 State Model.

The following Kalman filter equations closely follow [14]. The linear system model satisfies the stochastic differential equation:

$$\dot{\mathbf{x}}(t) = \mathbf{A}\mathbf{x}(t) + \mathbf{B}\mathbf{u}(t) + \mathbf{G}\mathbf{w}(t) \quad (2.5)$$

with state vector $\mathbf{x}(t)$, control input $\mathbf{u}(t)$ and system process noise $\mathbf{w}(t)$. The \mathbf{A} matrix gives the mathematical coupling between states and the \mathbf{G} matrix relates the system dynamics noise to the states. The dynamics noise $\mathbf{w}(t)$ is modeled as zero-mean white Gaussian noise with a noise strength \mathbf{Q} described by

$$\begin{aligned} \mathbb{E}[\mathbf{w}(t)] &= 0 \\ \mathbb{E}[\mathbf{w}(t)\mathbf{w}(t')^T] &= \mathbf{Q}(t)\delta(t - t') \end{aligned}$$

Integrating equation (2.5) gives the discrete-time form solution [14]:

$$\begin{aligned}\mathbf{x}_{i+1} &= \mathbf{\Phi}(t_{i+1}, t_i)\mathbf{x}_i + \int_{t_i}^{t_{i+1}} \mathbf{\Phi}(t_{i+1}, \tau)\mathbf{G}(\tau)\delta\boldsymbol{\beta}(\tau) \\ &= \mathbf{\Phi}(\Delta t)\mathbf{x}_i + \mathbf{w}_{d_i}\end{aligned}$$

where $\boldsymbol{\beta}(t)$ is a Brownian motion process with dispersion \mathbf{Q} , and $\mathbf{\Phi}$ is the discrete-time state transition matrix [14]. That is,

$$\mathbf{\Phi}(t_{i+1}, t_i) = \mathbf{\Phi}(\Delta t) = e^{\mathbf{A}\Delta t}$$

\mathbf{w}_{d_i} is a zero-mean, uncorrelated (i.e. white Gaussian) process with discretized noise strength \mathbf{Q}_{d_i} :

$$\begin{aligned}\mathbf{Q}_{d_i} &= \mathbb{E}[\mathbf{w}_{d_i}\mathbf{w}_{d_i}^T] \\ &= \int_{t_i}^{t_{i+1}} \mathbf{\Phi}(t_{i+1}, \tau)\mathbf{G}(\tau)\mathbf{Q}(\tau)\mathbf{G}(\tau)^T\mathbf{\Phi}(t_{i+1}, \tau)^T\delta\tau\end{aligned}$$

2.4.2 Measurement Model.

The Kalman filter accepts discrete-time measurements/observations, \mathbf{z} , from external sensors and incorporates them as part of its optimal estimate. Recall that the measurements must be uncorrelated both in time and with other measurements. The measurements must be of the linear form

$$\mathbf{z}_i = \mathbf{H}_i\mathbf{x}_i + \mathbf{v}_i$$

The \mathbf{H} matrix is the mathematical coupling between the system states in \mathbf{x} with the measurements in vector \mathbf{z} . The measurement noise vector, \mathbf{v} represents zero-mean white Gaussian noise with strength \mathbf{R} :

$$\mathbb{E}[\mathbf{v}_i\mathbf{v}_j^T] = \begin{cases} \mathbf{R}_i & \text{for } i = j \\ 0 & \text{for } i \neq j \end{cases}$$

2.4.3 Kalman Filter Algorithm.

As discussed above, the Kalman filter is developed using a model of the dynamic system, where a state transition matrix Φ_i , input matrix B_i , and noise vector w with strength Q_i are used to determine the state of the model. Given knowledge of the initial state and covariance estimates of the system, updates to state estimates can be calculated. State and covariance updates are designated by \hat{x} and P , respectively. The algorithm estimation is comprised of two phases: propagation and updating. In the propagation phase, the current state estimates are transitioned forward in time according to the system model. In the update phase, external measurement information is incorporated and the Kalman filter creates a new optimal estimate for the states using this information. State and covariance estimates updated by measurement z_i , are designated by a superscripted plus sign, \hat{x}^+ and P^+ , respectively. Similarly, state and covariance estimates propagated forward in time without measurement updates are designated by a superscripted minus sign, \hat{x}^- and P^- , respectively. Since the system and measurement models are stochastic, all states and measurements are treated as Gaussian random processes [12]. One of the unique properties of Gaussian random variables is that they can be completely described by their first two moments. Therefore, only the states' mean and covariance are calculated, propagated and updated during the Kalman filter phases.

The Kalman filter algorithm begins with initial conditions \hat{x}_{i-1}^+ and P_{i-1}^+ as inputs to the propagation phase. The propagation routine steps from time $i - 1$ to i . Φ_{i-1} , Q_{i-1} , B_{i-1} , and control input u are used to calculate \hat{x}_i^- and P_i^- according to

$$\begin{aligned}\hat{x}_i^- &= \Phi_{i-1}\hat{x}_{i-1}^+ + B_{i-1}u_{i-1} \\ P_i^- &= \Phi_{i-1}P_{i-1}^+ \Phi_{i-1}^T + G_d Q G_d^T\end{aligned}$$

\hat{x}_k^- and P_k^- are now the state and covariance estimates propagated forward to the next step. If no updated measurements are available, then the current state is reiterated through the measurement routine. If a measurement z is available, the update phase is initiated. The

state and covariance estimates from the propagation phase are used as inputs to the update phase. Given the modeled measurement matrix \mathbf{H}_i and measurement noise strength \mathbf{R}_i , the optimal Kalman gain \mathbf{K}_i is calculated as follows [14]:

$$\mathbf{K}_i = \mathbf{P}_i^- \mathbf{H}_i^T \left[\mathbf{H}_i \mathbf{P}_i^- \mathbf{H}_i^T + \mathbf{R}_i \right]^{-1}$$

The Kalman gain is then used to determine the amount of influence that the residual \mathbf{r} , discussed in detail below, will have on the updated state estimate $\hat{\mathbf{x}}_k^+$. A new covariance estimate \mathbf{P}_i^+ is also calculated using the optimal Kalman gain according to [14]:

$$\hat{\mathbf{x}}_i^+ = \hat{\mathbf{x}}_i^- + \mathbf{K}_i \mathbf{r}_i \quad (2.6)$$

$$\hat{\mathbf{P}}_i^+ = \hat{\mathbf{P}}_i^- - \mathbf{K}_i \mathbf{H}_i \hat{\mathbf{P}}_i^- \quad (2.7)$$

$$\mathbf{r}_i = \mathbf{z}_i - \mathbf{H}_i \hat{\mathbf{x}}_i^- \quad (2.8)$$

Both $\hat{\mathbf{x}}_i^+$ and \mathbf{P}_i^+ can be output as the updated estimates and utilized in the state propagation estimates. Prior to entering the propagation routine, the time index is reset and $\hat{\mathbf{x}}_i^+$ and \mathbf{P}_i^+ become $\hat{\mathbf{x}}_{i-1}^+$ and \mathbf{P}_{i-1}^+ . A summary of the Kalman filter algorithm is shown in Figure 2.2.

In a modeling and simulation setting, a truth model is used to refine the Kalman filter and improve its outputs. The difference between the model's truth and the Kalman filter is known as the error \mathbf{e}_i^+ [14].

$$\mathbf{e}_i^+ = \mathbf{x}_i - \hat{\mathbf{x}}_i^+ \quad (2.9)$$

Assuming the Kalman filter state estimates are Gaussian, then the error vector must also be Gaussian and completely described by its mean and covariance [14], [16].

$$\mathbb{E} [\mathbf{e}_i^+ | \mathbf{z}_i] = \hat{\mathbf{x}}_i^+ - \hat{\mathbf{x}}_i^+ = 0 \quad (2.10)$$

$$\mathbb{E} [\mathbf{e}_i^+ \mathbf{e}_i^{+T} | \mathbf{z}_i] = \mathbf{P}_i^+ \quad (2.11)$$

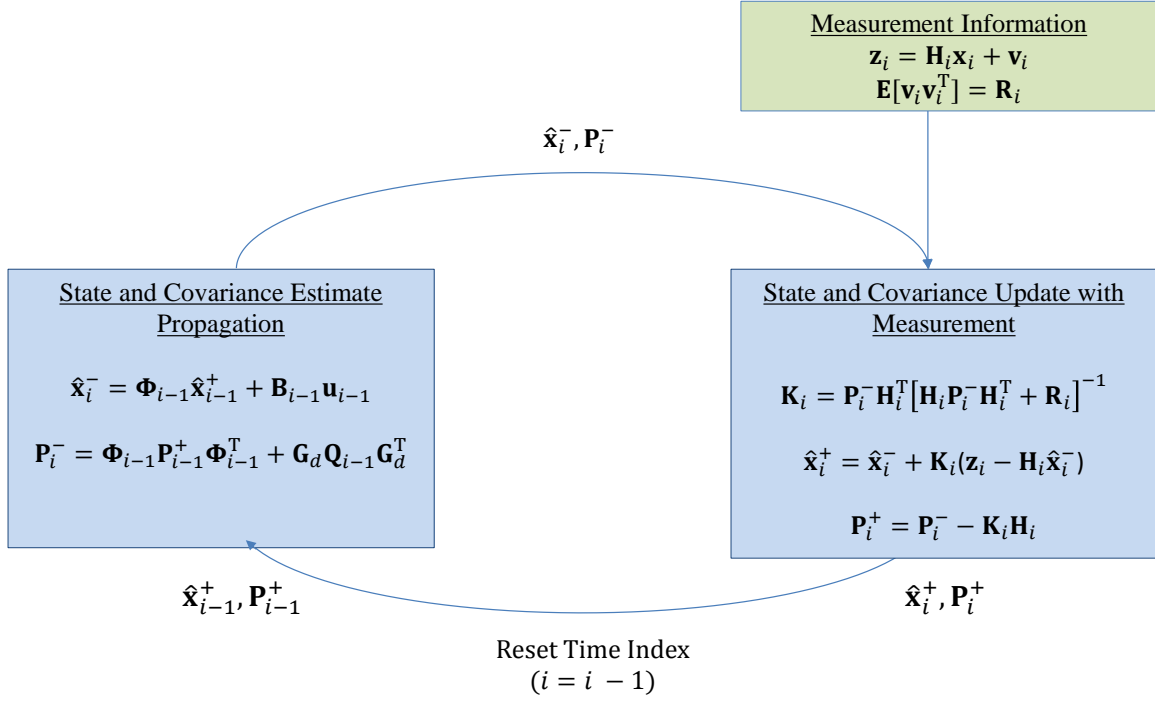


Figure 2.2: Kalman Filter Process [15]

The error covariance is completely independent of the measurements, but are dependent on the type and quality of the measurement [14]. For analysis in this thesis, the estimation error can be used to quantify the estimation algorithm's effectiveness.

In reality, the truth data is not known and must be measured. Noise is often introduced with actual measurements and must be weighed against the estimate of the next state. A residual is a comparison of the Kalman filter output to the measurement states. The residual is defined as the difference between the measurement and the state estimate prior to measurement update, as shown in equation (2.8). Residuals associated with the present state are independent of past residuals and are described as white, Gaussian, and zero mean

[16]. Like error, the residual can also be described by its mean and covariance as follows [14].

$$\mathbb{E} [\mathbf{r}_i] = 0 \quad (2.12)$$

$$\mathbb{E} [\mathbf{r}_i \mathbf{r}_i^T] = \mathbf{H}_i \mathbf{P}_i^- \mathbf{H}_i^T + \mathbf{R}_i \quad (2.13)$$

Given a nominally operating Kalman filter, residuals can be statistically monitored for changes, such as a bias shift. Significant changes typically indicate a malfunction or anomaly in the measurement, for example a failed sensor or “noisy” failure [14]. Figure 2.3 illustrates residual monitoring and sensor failure detection due to residual bias shift (top) and residual strength increase (bottom).

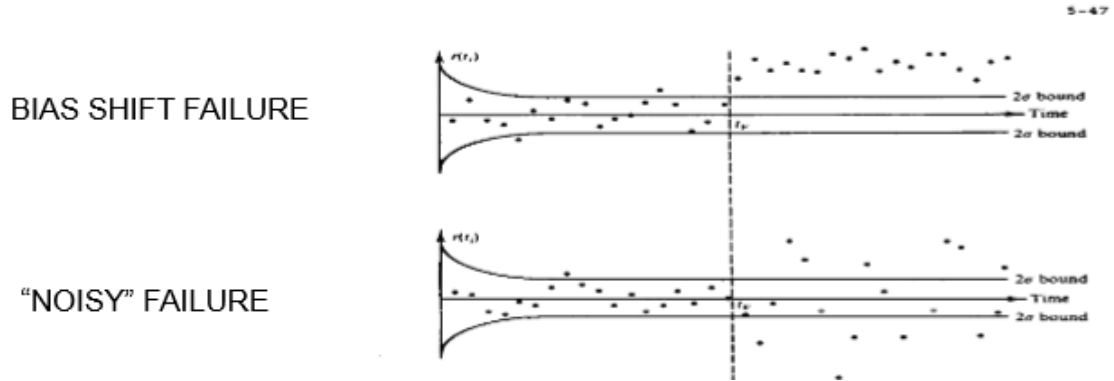


Figure 2.3: Residual Monitoring and Sensor Failure Detection [14]

As opposed to simulation studies, true states cannot be measured directly in practice. Therefore, it is difficult to determine if the Kalman filter is accurately estimating the states and whether the model is an accurate representation of reality. This uncertainty is mitigated by rigorous testing and simulation of the model by generating a simulated truth based on knowledge of how the system behaves dynamically and how measurements are reported. Chapter 3 will detail specifics of these system dynamics.

III. Algorithm Development and Model Creation

This chapter develops the INS and CAI accelerometer and gyroscope sensor models, the algorithm model used to integrate the CAI and INS measurements, and the navigation mechanization equations used for system simulation.

3.1 Postulate

In principle, the CAI-based acceleration measurement $u_k^{(CAI)}$ provided at the discrete time instant k at the completion of the k th duty cycle is the average acceleration during the CAI-based measurement interval. In other words, it is the area under the true acceleration divided by the CAI duty cycle length, $\alpha\Delta T$:

$$u_k^{(CAI)} = \frac{1}{\alpha\Delta T} \int_{(k-\alpha)\Delta T}^{k\Delta T} u(t)dt \quad (3.1)$$

where α is the CAI accelerometer or gyro duty cycle fraction, ΔT is the sampling time of the CAI-based acceleration measurements, and $u(t)$ is the true acceleration. Figure 3.1 illustrates the derivation for (3.1).

During the CAI accelerometer or gyro initiation time interval $[(k-1)\Delta T, (k-\alpha)\Delta T)$ in duty cycle k , there are $N-n$ conventional INS acceleration measurements u_{m_l} available, $l = 0, 1, \dots, N-n-1$. In addition, during the duty cycle interval $[(k-\alpha)\Delta T, k\Delta T)$, where the CAI accelerometer performs an acceleration measurement, there are $n+1$ measurements of the conventional INS, for $l = N-n, N-n+1, \dots, N$. N is the total number of acceleration measurements from the conventional INS during the CAI-based accelerometer's sampling time interval ΔT . Thus,

$$N \triangleq \frac{\Delta T}{\delta t} \quad (\gg 1)$$

where δt is the short sampling time of the conventional INS accelerometer. The number of conventional INS acceleration measurements taken while the CAI accelerometer is also

collecting a measurement is $n + 1$, as shown in Figure 3.1. Thus,

$$n \triangleq \frac{\alpha \Delta T}{\delta t}$$

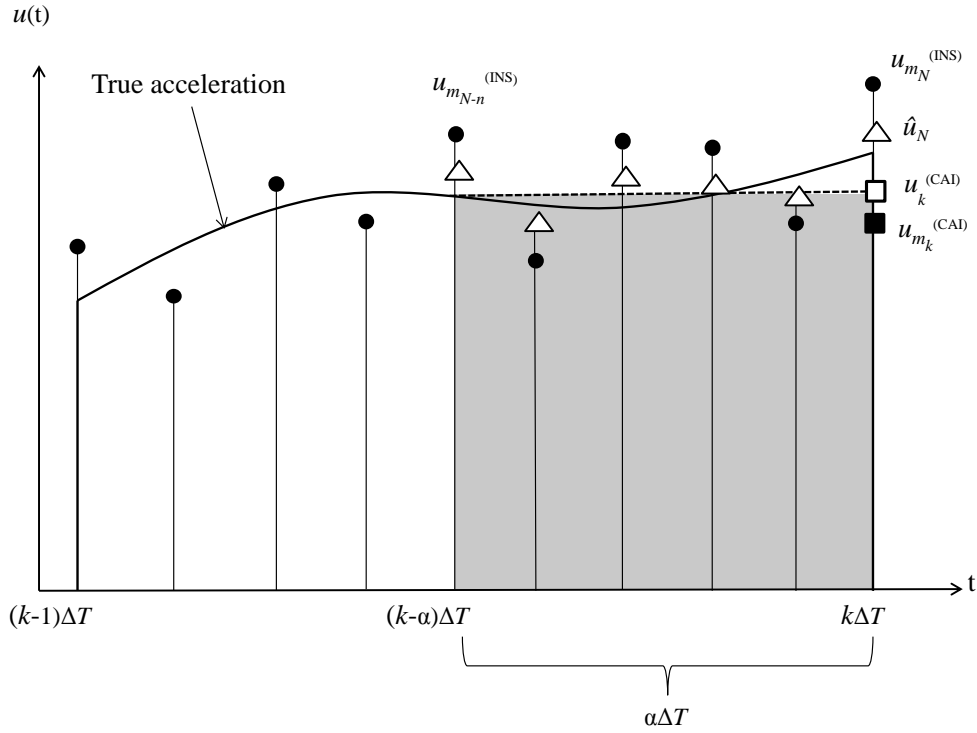


Figure 3.1: Model 1: Acceleration over one duty cycle (k)

The sampling intervals ΔT and δt of the CAI and conventional accelerometers, respectively, and the duty cycle fraction α , are such that both N and n are integers. The area, A , under the acceleration $u(t)$ during the duty cycle interval $[(k - \alpha)\Delta T \leq t \leq k\Delta T]$ is

approximated using the trapezoidal integration rule, as shown in the following equation:

$$\begin{aligned}
A &\approx \frac{1}{2} [u((k - \alpha)\Delta T) + u((k - \alpha)\Delta T + \delta t)] \delta t + \dots \\
&+ \frac{1}{2} [u(k\Delta T - \delta t) + u(k\Delta T)] \delta t \\
&= \left(\frac{u_{N-n} + u_N}{2} + \sum_{i=N-n+1}^{N-1} u_i \right) \delta t
\end{aligned} \tag{3.2}$$

where $u_i \equiv u(i \cdot \delta t)$.

The CAI-based accelerometer and gyro measurements are subject to drift. Each of the CAI accelerometer-provided acceleration samples $u_{m_k}^{(CAI)}$ has a small error caused by drift $\delta u_k^{(CAI)} \sim \mathcal{N}(0, \sigma_{CAI}^2)$. The quantification of the standard deviation of the sampling error σ_{CAI} is discussed in Appendix A. From (3.1) and (3.2), the true CAI measurement is obtained:

$$\begin{aligned}
u_{m_k}^{(CAI)} - \delta u_k^{(CAI)} &= \frac{1}{\alpha \Delta T} \int_{(k-\alpha)\Delta T}^{k\Delta T} u(t) dt \\
&= \frac{1}{n} \left(\frac{u_{N-n} + u_N}{2} + \sum_{i=N-n+1}^{N-1} u_i \right)
\end{aligned} \tag{3.3}$$

Expanding (3.3) gives

$$nu_{m_k}^{(CAI)} = \frac{1}{2} u_{N-n} + u_{N-n+1} + \dots + u_{N-1} + \frac{1}{2} u_N + \alpha N \delta u_k^{(CAI)} \tag{3.4}$$

While the acceleration measurement is exclusively discussed herein, the same also applies to the measurement of the aircraft's angular rate measured by the CAI-based gyros. In particular, σ_{CAI} would be substituted with the corresponding drift uncertainty for the CAI-based accelerometer ($\sigma_{v_d}^{(CAI)}$) and the CAI-based gyroscope ($\sigma_{\theta_d}^{(CAI)}$) discussed in Appendix A.

3.2 Signal Processing

Each of the acceleration and angular rate samples provided by the conventional INS accelerometers and gyros have a constant error from an unknown, random bias δu_b as well as error from drift $\delta u_i^{(INS)} \sim \mathcal{N}(0, \sigma_{INS}^2)$; obviously, $\sigma_{CAI} \ll \sigma_{INS}$. During the second half of each duty cycle $[N - n, \dots N]$, there are $n + 1$ acceleration measurements from the

conventional INS,

$$\left. \begin{aligned} u_{m_{N-n}}^{(INS)} &= u_{N-n} + \delta u_b + \delta u_{N-n}^{(INS)} \\ &\vdots \\ u_{m_N}^{(INS)} &= u_N + \delta u_b + \delta u_N^{(INS)} \end{aligned} \right\} \quad (3.5)$$

The conventional sensor's bias δu_b is recursively estimated. Thus, the estimate $\widehat{\delta u_b}^{(k)}$ of the bias δu_b changes for each duty cycle k according to the following definition:

$$\delta u_b \sim \mathcal{N}\left(\widehat{\delta u_b}^{(k)}, \left(\sigma_b^{(k)}\right)^2\right)$$

where $\sigma_b^{(k)}$ is the bias uncertainty. Since only the variance σ_b of the sensor's residual random bias is specified, the bias estimate is initialized with zero mean so that in duty cycle $k = 1$, $\delta u_b \sim \mathcal{N}(0, \sigma_b^2)$. Note that these error models would apply to both the acceleration and angular rate measurements; for simplicity, this discussion is limited to the accelerometer measurements along a single axis. The bias uncertainty specifications for the conventional INS accelerometers (σ_{b_A}) and gyros (σ_{b_G}) are calibrated in Appendix B to correspond to a 1 (km/hr) conventional navigation quality INS position error.

Equations (3.4) and (3.5) are combined to form a linear regression in the parameter Θ , yielding the measurement vector \mathbf{z} :

$$\mathbf{z} = \mathbf{H}\Theta + \mathbf{v} \quad (3.6)$$

where Θ is an $n + 1$ vector of true acceleration samples and the accelerometer's residual bias error δu_b as follows:

$$\Theta \triangleq \begin{bmatrix} u_{N-n} \\ \vdots \\ u_N \\ \delta u_b \end{bmatrix}_{(n+2) \times 1}$$

The associated regressor matrix, \mathbf{H} , is given as

$$\mathbf{H} = \begin{bmatrix} \mathbf{I}_{n+1} & \mathbf{e} \\ \mathbf{h}^T & 0 \\ \mathbf{0}_{1 \times (n+1)} & 1 \end{bmatrix}_{(n+3) \times (n+2)}$$

where \mathbf{I}_{n+1} is the $(n+1) \times (n+1)$ identity matrix, \mathbf{e} is a $(n+1) \times 1$ vector of ones, and the transpose of the vector \mathbf{h} is

$$\mathbf{h}^T = \left[\frac{1}{2} \quad 1 \quad \dots \quad 1 \quad \frac{1}{2} \right]_{1 \times (n+1)}$$

The measurement vector in the linear regression, \mathbf{z} , consists of the $n+1$ conventional INS measurements, the single CAI accelerometer measurement, and the bias error estimate available at the beginning of the current duty cycle, e.g. duty cycle k . \mathbf{z} is expressed as follows:

$$\mathbf{z} \triangleq \begin{bmatrix} u_{m_{N-n}}^{(INS)} \\ \vdots \\ u_{m_N}^{(INS)} \\ nu_{m_k}^{(CAI)} \\ \widehat{\delta u_b}^{(k-1)} \end{bmatrix}_{(n+3) \times 1}$$

The equation error vector in the linear regression, \mathbf{v} , is given by

$$\mathbf{v} = \begin{bmatrix} \delta u_{N-n}^{(INS)} \\ \vdots \\ \delta u_N^{(INS)} \\ n\delta u_k^{(CAI)} \\ \zeta_b^{(k-1)} \end{bmatrix}_{(n+3) \times 1} \quad (3.7)$$

where the residual variable $\xi_b^{(k-1)} \sim \mathcal{N}\left(0, \left(\sigma_b^{(k-1)}\right)^2\right)$. Thus equation (3.6) has a diagonal covariance matrix \mathbf{R} , expressed as follows [14]:

$$\begin{aligned} \mathbf{R} &\triangleq \mathbb{E}[\mathbf{v}\mathbf{v}^T] \\ &= \begin{bmatrix} \sigma_{INS}^2 \mathbf{I}_{n+1} & \mathbf{0}_{(n+1) \times 1} & \mathbf{0}_{(n+1) \times 1} \\ \mathbf{0}_{1 \times (n+1)} & n^2 \sigma_{CAI}^2 & 0 \\ \mathbf{0}_{1 \times (n+1)} & 0 & \left(\sigma_b^{(k-1)}\right)^2 \end{bmatrix}_{(n+3) \times (n+3)} \end{aligned} \quad (3.8)$$

Solving the linear regression in (3.6) according to the following equation for the optimal estimate vector $\widehat{\boldsymbol{\Theta}}$:

$$\widehat{\boldsymbol{\Theta}} = (\mathbf{H}^T \mathbf{R}^{-1} \mathbf{H})^{-1} \mathbf{H}^T \mathbf{R}^{-1} \mathbf{z} \quad (3.9)$$

yields the optimal estimates $\widehat{u}_{N-n}, \dots, \widehat{u}_N$ of the $n+1$ acceleration samples during the k th CAI duty cycle, $u((k-\alpha)\Delta T + i\delta t)$, $i = 0, \dots, n$ and the accelerometer's bias error estimate $\widehat{\delta u_b}^{(k)}$ obtained at the end of the k th CAI duty cycle. The covariance of the parameter estimation error is [14]:

$$\begin{aligned} \mathbf{P} &\triangleq \mathbb{E}[(\boldsymbol{\Theta} - \widehat{\boldsymbol{\Theta}})(\boldsymbol{\Theta} - \widehat{\boldsymbol{\Theta}})^T] \\ &= (\mathbf{H}^T \mathbf{R}^{-1} \mathbf{H})^{-1} \end{aligned} \quad (3.10)$$

recalling that $\widehat{\boldsymbol{\Theta}}$ from (3.9) is:

$$\widehat{\boldsymbol{\Theta}} = \left(\widehat{u}_{N-n}, \dots, \widehat{u}_N, \widehat{\delta u_b}^{(k)} \right)^T \quad (3.11)$$

Since the inputs u were treated as scalars, $\widehat{\boldsymbol{\Theta}}$ will need to be computed six times for each of the three acceleration and gyro measurements. However, the covariance matrix \mathbf{P} from the linear regression is the same for all acceleration components. Likewise, \mathbf{P} will be the same for all three angular rate components. Note that the bias uncertainty $\left(\sigma_b^{(k-1)}\right)^2$ featured in equation (3.8) is determined from \mathbf{P} as follows:

$$\left(\sigma_b^{(k)}\right)^2 = \mathbf{P}_{n+2, n+2}, \quad k = 2, \dots; \quad \sigma_b^{(1)} = \sigma_b$$

and is initialized at $k = 1$ from the respective accelerometer and gyroscope bias specifications, σ_{b_A} and σ_{b_G} , both derived in Appendix A. To calculate \mathbf{P} , substitute for the \mathbf{H} and \mathbf{R} matrices in (3.10):

$$\begin{aligned}
\mathbf{H}^T \mathbf{R}^{-1} \mathbf{H} &= \begin{bmatrix} \mathbf{I}_{n+1} & \mathbf{h} & \mathbf{0}_{(n+1) \times 1} \\ \mathbf{e}^T & 0 & 1 \end{bmatrix} \begin{bmatrix} \frac{1}{\sigma_{INS}^2} \mathbf{I}_{n+1} & \mathbf{0}_{(n+1) \times 1} & \mathbf{0}_{(n+1) \times 1} \\ \mathbf{0}_{1 \times (n+1)} & \frac{1}{n^2 \sigma_{CAI}^2} & 0 \\ \mathbf{0}_{1 \times (n+1)} & 0 & \frac{1}{(\sigma_b^{(k-1)})^2} \end{bmatrix} \begin{bmatrix} \mathbf{I}_{n+1} & \mathbf{e} \\ \mathbf{h}^T & 0 \\ \mathbf{0}_{1 \times (n+1)} & 1 \end{bmatrix} \\
&= \begin{bmatrix} \mathbf{I}_{n+1} & \mathbf{h} & \mathbf{0}_{(n+1) \times 1} \\ \mathbf{e}^T & 0 & 1 \end{bmatrix} \begin{bmatrix} \frac{1}{\sigma_{INS}^2} \mathbf{I}_{n+1} & \frac{1}{\sigma_{INS}^2} \mathbf{e} \\ \frac{1}{n^2 \sigma_{CAI}^2} \mathbf{h}^T & 0 \\ \mathbf{0}_{1 \times (n+1)} & \frac{1}{(\sigma_b^{(k-1)})^2} \end{bmatrix} \\
&= \begin{bmatrix} \frac{1}{\sigma_{INS}^2} \mathbf{I}_{n+1} + \frac{1}{n^2 \sigma_{CAI}^2} \mathbf{h} \mathbf{h}^T & \frac{1}{\sigma_{INS}^2} \mathbf{e} \\ \frac{1}{\sigma_{INS}^2} \mathbf{e}^T & \frac{n+1}{\sigma_{INS}^2} + \frac{1}{(\sigma_b^{(k-1)})^2} \end{bmatrix}_{(n+2) \times (n+2)} \quad (3.12)
\end{aligned}$$

Since (3.12) is in block form, use

Lemma 1: Assume \mathbf{A} is symmetric and invertible. The inverse of the blocked matrix

$$\begin{bmatrix} \mathbf{A} & \mathbf{b} \\ \mathbf{b}^T & c \end{bmatrix}^{-1} = \begin{bmatrix} \mathbf{A}^{-1} + \frac{1}{d} \mathbf{A}^{-1} \mathbf{b} \mathbf{b}^T \mathbf{A}^{-1} & -\frac{1}{d} \mathbf{A}^{-1} \mathbf{b} \\ -\frac{1}{d} \mathbf{b}^T \mathbf{A}^{-1} & \frac{1}{d} \end{bmatrix} \quad (3.13)$$

where the scalar $d = c - \mathbf{b}^T \mathbf{A}^{-1} \mathbf{b}$. □

From (3.12):

$$\begin{aligned}\mathbf{A} &= \frac{1}{\sigma_{INS}^2} \mathbf{I}_{n+1} + \frac{1}{n^2 \sigma_{CAI}^2} \mathbf{h} \mathbf{h}^T \\ \mathbf{b} &= \frac{1}{\sigma_{INS}^2} \mathbf{e} \\ c &= \frac{n+1}{\sigma_{INS}^2} + \frac{1}{\left(\sigma_b^{(k-1)}\right)^2} \\ d &= \frac{n+1}{\sigma_{INS}^2} + \frac{1}{\left(\sigma_b^{(k-1)}\right)^2} - \frac{1}{\sigma_{INS}^4} \mathbf{e}^T \mathbf{A}^{-1} \mathbf{e}\end{aligned}$$

To solve for \mathbf{A}^{-1} , use the following Matrix Inversion Lemma (MIL):

MIL: Assume the dimensions of the relevant matrices are compatible and the required matrix inverses exist. Then,

$$(\mathbf{A}_1 - \mathbf{A}_2 \mathbf{A}_4^{-1} \mathbf{A}_3)^{-1} = \mathbf{A}_1^{-1} + \mathbf{A}_1^{-1} \mathbf{A}_2 (\mathbf{A}_4 - \mathbf{A}_3 \mathbf{A}_1^{-1} \mathbf{A}_2)^{-1} \mathbf{A}_3 \mathbf{A}_1^{-1} \quad \square$$

Set

$$\mathbf{A}_1 = \frac{1}{\sigma_{INS}^2} \mathbf{I}_{n+1}$$

$$\mathbf{A}_2 = \mathbf{h}$$

$$\mathbf{A}_3 = \mathbf{h}^T$$

$$\mathbf{A}_4 = -n^2 \sigma_{CAI}^2$$

which gives the inverse of \mathbf{A} :

$$\begin{aligned}\mathbf{A}^{-1} &= \sigma_{INS}^2 \mathbf{I}_{n+1} - \sigma_{INS}^2 \mathbf{I}_{n+1} \mathbf{h} (n^2 \sigma_{CAI}^2 + \mathbf{h}^T \sigma_{INS}^2 \mathbf{I}_{n+1} \mathbf{h})^{-1} \mathbf{h}^T \sigma_{INS}^2 \mathbf{I}_{n+1} \\ &= \sigma_{INS}^2 \mathbf{I}_{n+1} - \frac{\sigma_{INS}^4}{n^2 \sigma_{CAI}^2 + \sigma_{INS}^2 \mathbf{h}^T \mathbf{h}} \mathbf{h} \mathbf{h}^T\end{aligned}$$

Substituting the above expressions gives the covariance of the parameter's estimation error in (3.10).

Finally, inserting the calculated covariance of the parameter's estimation error, \mathbf{P} , into equation (3.9) gives the accelerations' estimate and current accelerometer's bias estimate:

$$\widehat{\boldsymbol{\Theta}} = \mathbf{P} \begin{bmatrix} \mathbf{I}_{n+1} & \mathbf{h} & \mathbf{0}_{(n+1) \times 1} \\ \mathbf{e}^T & 0 & 1 \end{bmatrix} \begin{bmatrix} \frac{1}{\sigma_{INS}^2} \mathbf{I}_{n+1} & \mathbf{0}_{(n+1) \times 1} & \mathbf{0}_{(n+1) \times 1} \\ \mathbf{0}_{1 \times (n+1)} & \frac{1}{n^2 \sigma_{CAI}^2} & 0 \\ \mathbf{0}_{1 \times (n+1)} & 0 & \frac{1}{(\sigma_b^{(k-1)})^2} \end{bmatrix} \mathbf{z}$$

Substitution gives

$$\widehat{\boldsymbol{\Theta}} = \begin{bmatrix} \frac{1}{\sigma_{INS}^2} \left[\mathbf{A}^{-1} + \frac{1}{d} (\mathbf{A}^{-1} \mathbf{b} \mathbf{b}^T \mathbf{A}^{-1} - \mathbf{A}^{-1} \mathbf{b} \mathbf{e}^T) \right] & \frac{1}{n^2 \sigma_{CAI}^2} \left(\mathbf{A}^{-1} + \frac{1}{d} \mathbf{A}^{-1} \mathbf{b} \mathbf{b}^T \mathbf{A}^{-1} \right) \mathbf{h} & \frac{-1}{d (\sigma_b^{(k-1)})^2} \mathbf{A}^{-1} \mathbf{b} \\ \frac{-1}{d \sigma_{INS}^2} (\mathbf{b}^T \mathbf{A}^{-1} - \mathbf{e}^T) & \frac{-1}{d n \sigma_{CAI}^2} \mathbf{b}^T \mathbf{A}^{-1} \mathbf{h} & \frac{1}{d (\sigma_b^{(k-1)})^2} \end{bmatrix} \mathbf{z}$$

where

$$\begin{aligned} \mathbf{A}^{-1} \mathbf{b} &= \sigma_{INS}^2 \mathbf{b} - \frac{\sigma_{INS}^4}{n^2 \sigma_{CAI}^2 + \sigma_{INS}^2} \mathbf{h} \mathbf{h}^T \mathbf{b} \\ &= \mathbf{e} - \frac{n \sigma_{INS}^2}{n^2 \sigma_{CAI}^2 + \sigma_{INS}^2 (n - \frac{1}{2})} \mathbf{h} \end{aligned}$$

To solve for $\frac{1}{d}$, first expand d

$$\begin{aligned} d &= \frac{n+1}{\sigma_{INS}^2} + \frac{1}{(\sigma_b^{(k-1)})^2} - \frac{1}{\sigma_{INS}^4} \left((n+1) \sigma_{INS}^2 - \frac{n^2 \sigma_{INS}^4}{n^2 \sigma_{CAI}^2 + \sigma_{INS}^2} \mathbf{h}^T \mathbf{h} \right) \\ &= \frac{1}{(\sigma_b^{(k-1)})^2} + \frac{n^2}{n^2 \sigma_{CAI}^2 + \sigma_{INS}^2 (n - \frac{1}{2})} \end{aligned}$$

Then invert d as follows:

$$\frac{1}{d} = \frac{(\sigma_b^{(k-1)})^2 (n^2 \sigma_{CAI}^2 + (n - \frac{1}{2}) \sigma_{INS}^2)}{n^2 \sigma_{CAI}^2 + n^2 (\sigma_b^{(k-1)})^2 + (n - \frac{1}{2}) \sigma_{INS}^2} \quad (3.14)$$

Concerning the recursion for $\sigma_b^{(k)}$:

$$(\sigma_b^{(k)})^2 = \frac{1}{d}$$

Then from equation (3.14)

$$\sigma_b^{(k)} = \sqrt{\frac{n^2 \sigma_{CAI}^2 + \left(n - \frac{1}{2}\right) \sigma_{INS}^2}{n^2 \sigma_{CAI}^2 + n^2 \left(\sigma_b^{(k-1)}\right)^2 + \left(n - \frac{1}{2}\right) \sigma_{INS}^2}} \cdot \sigma_b^{(k-1)}$$

Evidently, $\sigma_b^{(k)}$ is monotonically decreasing.

Having solved the linear regression in (3.9) to obtain the estimates $\widehat{u}_n, \dots, \widehat{u}_N$ of the scalar sensor inputs u_n, \dots, u_N and the current estimate of the input bias $\widehat{u}_b^{(k)}$, the error δu_i is determined by substituting (3.6) into (3.9):

$$\widehat{\Theta} - \Theta = (\mathbf{H}^T \mathbf{R}^{-1} \mathbf{H})^{-1} \mathbf{H}^T \mathbf{R}^{-1} \mathbf{v}$$

Since the first $n + 1$ elements of $\Theta \in \mathbb{R}^{n+2}$ consists of u_n, \dots, u_N , it is now known that

$$\begin{aligned} \delta u_i &\triangleq \widehat{u}_i - u_i \\ &= \mathbf{e}_{i+1-n}^T (\mathbf{H}^T \mathbf{R}^{-1} \mathbf{H})^{-1} \mathbf{H}^T \mathbf{R}^{-1} \mathbf{v}, \quad i = n, \dots, N \end{aligned}$$

where \mathbf{e}_j is the $n + 2$ vector, all of whose elements are zero except the j -th element, which is 1. Recall that the elements of the $n + 3$ equation error vector \mathbf{v} in (3.7) consist of the errors in the $n + 2$ measurements taken during the CAI measurement part of the duty cycle and the last element $\zeta_b^{(k-1)}$ is the current knowledge of the residual uncertainty (computed at the end of the $k - 1$ duty cycle) of the bias error δu_b .

Indeed, at the beginning of the current, k th duty cycle, information concerning the bias error is supplied as follows:

$$\delta u_b \sim \mathcal{N}\left(\widehat{\delta u}_b^{(k-1)}, \left(\sigma_b^{(k-1)}\right)^2\right)$$

Furthermore, the statistics of $\zeta_b^{(k-1)}$ are expressed as follows:

$$\zeta_b^{(k-1)} \sim \mathcal{N}\left(0, \left(\sigma_b^{(k-1)}\right)^2\right) \quad (3.15)$$

Hence, $\delta u_i = \alpha_i \cdot \zeta_b^{(k-1)} + [\text{a linear combination of the first } n + 2 \text{ elements of } \mathbf{v}]$ where the coefficients α_i are expressed as follows:

$$\alpha_i = \mathbf{e}_{i+1-n} (\mathbf{H}^T \mathbf{R}^{-1} \mathbf{H})^{-1} \mathbf{H}^T \mathbf{R}^{-1} \mathbf{e}_{n+3}, \quad i = n, \dots, N \quad (3.16)$$

3.3 Proof of Concept

The combined acceleration and angular rate estimates, $\widehat{\Theta}$, during the CAI measurement interval $[(k-1)\Delta T, k\Delta T]$ and the conventional INS acceleration and angular rate measurements prior to the interval are used in an inertial frame INS to calculate the velocity and position x of the aircraft. This is accomplished by integrating according to the simple kinematic differential equation:

$$\ddot{x} = u$$

where u is the measured acceleration. The angular rotation θ is calculated by integrating the angular rate ω as follows:

$$\dot{\theta} = \omega$$

The error in position is caused by the accelerometer bias \mathbf{b}_A and any platform misalignment that may be present. The misalignment of the platform due to the gyroscopes' errors is caused by the gyro bias \mathbf{b}_G .

The position and velocity estimation errors are determined by the conventional and CAI accelerometer drifts (σ_{INS} and σ_{CAI} , respectively), and the bias \mathbf{b}_A of the conventional accelerometer. Specifically, the drift induced error prior to the CAI accelerometer measurement duty cycle is determined by σ_{INS} , and the drift induced error during the CAI duty cycle interval is determined from the covariance matrix \mathbf{P} in equation (3.10). Similarly, the angular rotation errors are determined from the corresponding INS and CAI gyro drifts and gyro bias \mathbf{b}_G . The $(n+2) \times (n+2)$ covariance matrix \mathbf{P} is not diagonal. Further analysis is required to correctly account for the correlation terms in \mathbf{P} and solve for the variance of the navigation state error caused by the acceleration and gyroscope measurement errors. For both the INS and CAI IMUs, the accelerometer error equations are as follows:

$$\delta\ddot{x} = \delta u, \quad \delta\dot{u} = 0$$

The gyroscope error equation is:

$$\delta\dot{\theta} = \delta\omega$$

3.4 Navigation

A wings level flight at constant altitude is considered. For proof of concept, the Earth is assumed flat and non-rotating and the inertial navigation frame is attached to the Earth. The simplified discrete-time navigation state error equations are derived from their continuous-time form as follows [17]:

$$\delta\dot{\mathbf{x}}_c(t) = \mathbf{M}_c\delta\mathbf{x}_c(t) + \mathbf{\Gamma}_c \begin{bmatrix} \mathbf{b}_A \\ \mathbf{b}_G \end{bmatrix} + \mathbf{\Gamma}_c \begin{bmatrix} \sigma_{v_e}\dot{\boldsymbol{\beta}}_A(t) \\ \sigma_{\theta_e}\dot{\boldsymbol{\beta}}_G(t) \end{bmatrix} \quad (3.17)$$

where the navigation state is

$$\mathbf{x}_c = \begin{bmatrix} x, y, z, v_x, v_y, v_z, \phi, \theta, \psi \end{bmatrix}^T$$

for aircraft position coordinates x, y, z ; velocities v_x, v_y, v_z , and Euler angles ϕ, θ, ψ . The continuous time state space matrices \mathbf{M}_c and $\mathbf{\Gamma}_c$ are given as:

$$\mathbf{M}_c = \begin{bmatrix} \mathbf{0} & \mathbf{I} & \mathbf{0} \\ \mathbf{0} & \mathbf{0} & \mathbf{F} \\ \mathbf{0} & \mathbf{0} & \mathbf{0} \end{bmatrix}_{9 \times 9}, \quad \mathbf{\Gamma}_c = \begin{bmatrix} \mathbf{0} & \mathbf{0} \\ \mathbf{C}_n^b & \mathbf{0} \\ \mathbf{0} & -\mathbf{C}_n^b \end{bmatrix}_{9 \times 6}$$

The matrix $\mathbf{F} = \mathbf{f} \times$ is the skew symmetric matrix form of the nominal specific force vector \mathbf{f} . During wings level flight, \mathbf{f} is as follows:

$$\mathbf{f} = \begin{bmatrix} u_x \\ 0 \\ g \end{bmatrix}$$

where u_x is the aircraft's longitudinal acceleration and g is the acceleration of gravity. Consequently, the matrix \mathbf{F} is as follows:

$$\mathbf{F} = \mathbf{f} \times = \begin{bmatrix} 0 & -g & 0 \\ g & 0 & -u_x \\ 0 & u_x & 0 \end{bmatrix}$$

\mathbf{C}_n^b is the 3×3 Direction Cosine Matrix (DCM) and for small Euler angles is as follows:

$$\mathbf{C}_n^b = \begin{bmatrix} 1 & -\psi & \theta \\ \psi & 1 & -\phi \\ -\theta & \phi & 1 \end{bmatrix}$$

For constant altitude, wings level flight in the x axis direction, \mathbf{C}_n^b is nominally the identity matrix, \mathbf{I} . $\boldsymbol{\beta}_A$ and $\boldsymbol{\beta}_G$ are 3×1 vectors of independent, unity Brownian motions, that is, $\boldsymbol{\beta}_A(t) \sim \mathcal{N}(0, t \cdot \mathbf{I})$ and $\boldsymbol{\beta}_G(t) \sim \mathcal{N}(0, t \cdot \mathbf{I})$. The rate gyro drift parameter σ_{θ_c} is derived from the rate gyro's drift specification in Appendix A.

Converting the dynamics in (3.17) to discrete time, the navigation state discrete-time error equation is

$$\delta \mathbf{x}_{i+1} = \mathbf{M}_d \delta \mathbf{x}_i + \mathbf{\Gamma}_d \begin{bmatrix} \mathbf{b}_A \\ \mathbf{b}_G \end{bmatrix} + \mathbf{\Gamma}_c \begin{bmatrix} \sigma_{v_d} \mathbf{w}_{A_i} \\ \sigma_{\theta_d} \mathbf{w}_{G_i} \end{bmatrix} \quad (3.18)$$

where

$$\mathbf{M}_d = e^{\mathbf{M}_c \Delta T} = \begin{bmatrix} \mathbf{I} & \mathbf{I} \Delta T & -\frac{1}{2} \mathbf{F} \Delta T^2 \\ \mathbf{0} & \mathbf{I} & -\mathbf{F} \Delta T \\ \mathbf{0} & \mathbf{0} & \mathbf{I} \end{bmatrix}_{9 \times 9},$$

$$\begin{aligned}
\mathbf{\Gamma}_d &= \int_0^{\Delta T} e^{\mathbf{M}_c(t-\tau)} \mathbf{\Gamma}_c d\tau \\
&= \mathbf{M}_d \cdot \left(\int_0^{\Delta T} e^{\mathbf{M}_c(-\tau)} d\tau \right) \cdot \mathbf{\Gamma}_c \\
&= \begin{bmatrix} \frac{1}{2} \mathbf{I} \Delta T^2 & -\frac{1}{6} \mathbf{F} \Delta T^3 \\ \mathbf{I} \Delta T & -\frac{1}{2} \mathbf{F} \Delta T^2 \\ \mathbf{0} & \mathbf{I} \Delta T \end{bmatrix}_{9 \times 6}
\end{aligned}$$

and $\mathbf{w}_{A_i} \sim \mathcal{N}(0, \mathbf{I})$, $\mathbf{w}_{G_i} \sim \mathcal{N}(0, \mathbf{I})$. The discrete-time accelerometer and gyro parameter featured in (3.18), σ_{v_d} and σ_{θ_d} respectively, are derived in Appendix A.

It is herein assumed that initially the INS is perfectly aligned (no alignment error) and therefore the navigation state error is exclusively brought about by the accelerometers' and gyros' biases and drifts. As such, the navigation state error's statistics will be determined by the accelerometers' and gyros' bias statistics and the intensity of their respective drifts.

After the measurement part of the k th duty cycle is complete and the linear regression in (3.9) has been solved, one reruns the mechanization equations which are modified as follows:

$$\mathbf{x}_{m_{i+}} = f_d(\mathbf{x}_{m_i}, \widehat{\mathbf{u}}_i), \quad i = n, \dots, N-1 \quad (3.19)$$

where $\widehat{\mathbf{u}}_i$ is a 6×1 vector of the scalar accelerometer and gyro estimates $\widehat{u}_n, \dots, \widehat{u}_{N-1}$ obtained from (3.9). The result is a smoothed navigation state estimate $\mathbf{x}_{m_{n+1}}, \dots, \mathbf{x}_{m_N}$ for the CAI measurement portion of the duty cycle. The navigation state filtered estimate \mathbf{x}_{m_N} is obtained in real time with some computational delay; however, the smoothed navigation state estimates $\mathbf{x}_{m_{N-1}}, \dots, \mathbf{x}_{m_{n+1}}$ are delayed by the computational delay $+ \delta t, \dots, (n-1)\delta t$, where δt are the discrete-time instants. In view of the mechanization equation expressed in (3.19), the discrete-time navigation state error $\delta \mathbf{x}_{m_{i+1}}$ for the smoothed navigation state during the CAI measurement part of the duty cycle is expressed as follows:

$$\delta \mathbf{x}_{m_{i+1}} = \mathbf{M}_d \delta \mathbf{x}_{m_i} + \mathbf{\Gamma}_d \delta \mathbf{u}_i, \quad i = n, \dots, N-1 \quad (3.20)$$

where

$$\delta \mathbf{x}_{m_i} = \mathbf{x}_{m_i} - \mathbf{x}_i, \quad i = n + 1, \dots, N$$

$$\delta \mathbf{u}_i = \widehat{\mathbf{u}}_i - \mathbf{u}_i, \quad i = n, \dots, N - 1$$

and $\delta \mathbf{x}_{m_i}$ and $\delta \mathbf{u}_i$ are 6×1 vectors of the scalar accelerometer and gyro measurement errors. The statistics of the scalar input errors $\delta u_n, \dots, \delta u_{N-1}$ are provided from the solution to the linear regression in (3.10) obtained at the completion of the k th duty cycle, and are as follows:

$$\begin{bmatrix} \delta u_n \\ \vdots \\ \delta u_N \\ \zeta_b^{(k)} \end{bmatrix} \sim \mathcal{N}(0, \mathbf{P}^{(k)})$$

The covariance of the smoothed navigation state estimation error $\mathbf{P}^{(\delta x)}$, expressed in (3.20), may be rewritten as follows:

$$\delta \mathbf{x}_{m_j} = \mathbf{M}_d^{j-n} \delta \mathbf{x}_{m_n} + \sum_{l=1}^{j-n} \mathbf{M}_d^{j-n-l} \mathbf{\Gamma}_d \delta \mathbf{u}_{n+l-1}, \quad j = n + 1, \dots, N \quad (3.21)$$

where $\delta \mathbf{x}_{m_n} \sim \mathcal{N}(0, \mathbf{P}_n^{(\delta x)})$. The covariance of the smoothed navigation state estimation error $\mathbf{P}_{n+1}^{(\delta x)}, \dots, \mathbf{P}_N^{(\delta x)}$ is then expressed as:

$$\begin{aligned} \mathbf{P}_{n+1}^{(\delta x)} &\equiv \mathbb{E}(\delta \mathbf{x}_{m_{n+1}} \delta \mathbf{x}_{m_{n+1}}^T) = \mathbf{M}_d \mathbf{P}_n^{(\delta x)} \mathbf{M}_d^T + \mathbf{\Gamma}_d \mathbf{P}_{1,1}^{(k)} \mathbf{\Gamma}_d^T + \mathbf{M}_d \mathbb{E}(\delta \mathbf{x}_{m_n} \delta \mathbf{u}_n^T) \mathbf{\Gamma}_d^T \\ &\quad + \mathbf{\Gamma}_d \left(\mathbb{E}(\delta \mathbf{x}_{m_n} \delta \mathbf{u}_n^T) \right)^T \mathbf{M}_d^T \\ &\quad \vdots \\ \mathbf{P}_N^{(\delta x)} &\equiv \mathbb{E}(\delta \mathbf{x}_{m_N} \delta \mathbf{x}_{m_N}^T) \end{aligned}$$

To solve for the covariances $\mathbb{E}(\delta \mathbf{x}_{m_n} \delta \mathbf{u}_i^T)$ when $i = n, \dots, N - 1$, $\delta \mathbf{x}_{m_n}$ must first be considered. For the first half of each duty cycle (prior to the CAI measurement portion),

the mechanization equation for the CAI-aided INS is expressed as follows:

$$\mathbf{x}_{m_{i+1}} = f_d(\mathbf{x}_{m_i}, \mathbf{u}_{m_i}^{(INS)} - \widehat{\mathbf{u}}_b^{(k-1)})$$

The discrete time navigation state error equation is:

$$\delta \mathbf{x}_{m_{i+1}} = \mathbf{M}_d \delta \mathbf{x}_{m_i} + \mathbf{\Gamma}_d \boldsymbol{\zeta}_{b_i}^{(k-1)} + \mathbf{\Gamma}_c \begin{bmatrix} \sigma_{v_d} \mathbf{w}_{A_i} \\ \sigma_{\theta_d} \mathbf{w}_{G_i} \end{bmatrix}, \quad i = 0, \dots, n-1$$

where $\boldsymbol{\zeta}_{b_i}^{(k-1)}$ is a 6×1 vector of the scalar residual uncertainties, defined by (3.15), of the accelerometer and gyro bias errors. Note that $\boldsymbol{\zeta}_{b_{i+1}}^{(k-1)} = \boldsymbol{\zeta}_{b_i}^{(k-1)}$. Thus

$$\delta \mathbf{x}_{m_n} = \mathbf{M}_d^n \delta \mathbf{x}_{m_0} + \left(\sum_{l=0}^{n-1} \mathbf{M}_d^l \right) \mathbf{\Gamma}_d \boldsymbol{\zeta}_b^{(k-1)} + \mathbf{\Gamma}_c \begin{bmatrix} \sigma_{v_d} \mathbf{w}_{A_i} \\ \sigma_{\theta_d} \mathbf{w}_{G_i} \end{bmatrix}$$

The correlations $\mathbb{E}(\delta \mathbf{x}_n \delta \mathbf{u}_i^T)$ for $i = n, \dots, N-1$ can then be calculated as follows:

$$\begin{aligned} \mathbb{E}(\delta \mathbf{x}_n \delta \mathbf{u}_i^T) &= \left(\sum_{l=0}^{n-1} \mathbf{M}_d^l \right) \mathbf{\Gamma}_d \mathbb{E}(\boldsymbol{\zeta}_b^{(k-1)} \alpha_i \boldsymbol{\zeta}_b^{(k-1)}) \\ &= \alpha_i (\sigma_b^{k-1})^2 \left(\sum_{l=0}^{n-1} \mathbf{M}_d^l \right) \mathbf{\Gamma}_d \end{aligned}$$

where α_i was given in (3.16).

Returning to (3.18), if it is assumed that the accelerometer and gyro errors \mathbf{b}_A and \mathbf{b}_G respectively are constant, random Gaussian distributed biases, the state error vector $\delta \mathbf{x}$ may be augmented with the vectors \mathbf{b}_A and \mathbf{b}_G as follows:

$$\delta \mathbf{x}_i = \left[\delta x_i, \delta y_i, \delta z_i, \delta v_{x_i}, \delta v_{y_i}, \delta v_{z_i}, \delta \phi_i, \delta \theta_i, \delta \psi_i, \mathbf{b}_{A_i}, \mathbf{b}_{G_i} \right]^T$$

Consequently, the dynamics matrix is augmented with discrete time matrix $\mathbf{\Gamma}_d$ as follows:

$$\mathbf{A} = \begin{bmatrix} \mathbf{M}_d & \mathbf{\Gamma}_d \\ \mathbf{0}_{6 \times 9} & \mathbf{I}_{6 \times 6} \end{bmatrix}_{15 \times 15}$$

and $\mathbf{\Gamma}_c$ is augmented to acknowledge the additional bias states to form discrete time matrix \mathbf{G} :

$$\mathbf{G} = \begin{bmatrix} \mathbf{\Gamma}_c \\ \mathbf{0}_{6 \times 6} \end{bmatrix} = \begin{bmatrix} \mathbf{0} & \mathbf{0} \\ \mathbf{I} & \mathbf{0} \\ \mathbf{0} & \mathbf{I} \\ \mathbf{0} & \mathbf{0} \\ \mathbf{0} & \mathbf{0} \end{bmatrix}_{15 \times 6}$$

The final discrete-time form of the augmented navigation state error dynamics is expressed as follows:

$$\delta \mathbf{x}_{i+1} = \mathbf{A} \delta \mathbf{x}_i + \mathbf{G} \sqrt{\mathbf{Q}} \mathbf{w}_i$$

where

$$\sqrt{\mathbf{Q}} = \begin{bmatrix} \sigma_{v_d} \mathbf{I} & \mathbf{0} \\ \mathbf{0} & \sigma_{\theta_d} \mathbf{I} \end{bmatrix}_{6 \times 6}, \mathbf{w}_i = \begin{bmatrix} \mathbf{w}_{A_i} \\ \mathbf{w}_{G_i} \end{bmatrix}_{6 \times 1}$$

3.5 Simulation

For simulation of the conventional INS, (3.18) is modified slightly to reflect the calibration performed in Appendix B as follows:

$$\delta \mathbf{x}_{i+1} = \mathbf{M}_d \delta \mathbf{x}_i + \mathbf{\Gamma}_d \begin{bmatrix} \mathbf{b}_A \\ \mathbf{b}_G \end{bmatrix} + \mathbf{\Gamma}_d \begin{bmatrix} \sigma_{v_d} \mathbf{w}_{A_i} \\ \sigma_{\theta_d} \mathbf{w}_{G_i} \end{bmatrix} \quad (3.22)$$

where the accelerometer and gyro errors \mathbf{b}_A and \mathbf{b}_G are 3×1 vectors of constant, random Gaussian distributed bias, so $\mathbf{b}_A \sim \mathcal{N}(0, \sigma_{b_A}^2 \mathbf{I})$ and $\mathbf{b}_G \sim \mathcal{N}(0, \sigma_{b_G}^2 \mathbf{I})$. The values for the bias variances, $\sigma_{b_A}^2$ and $\sigma_{b_G}^2$, and discrete-time accelerometer and gyro parameters, σ_{v_d} and σ_{θ_d} respectively, are calculated in Appendix B.

The CAI-aided INS simulation mechanization equations for the first $N - n$ measurements of each duty cycle $k = 1, \dots, 3600$ are as follows:

$$\delta \mathbf{x}_{m_{i+1}} = \mathbf{M}_d \delta \mathbf{x}_{m_i} + \mathbf{\Gamma}_d \left(\mathbf{u}_{m_i}^{(INS)} - \widehat{\delta \mathbf{u}_b}^{(k-1)} \right), \quad \delta \mathbf{x}_{m_0} = \mathbf{0} \in \mathbb{R}^9, \quad i = 0, \dots, N - n - 1 \quad (3.23)$$

where $\mathbf{u}_{m_i}^{(INS)}$ is a 6×1 vector consisting of each scalar conventional INS accelerometer and gyro measurement described in (3.5). Likewise, $\widehat{\delta \mathbf{u}_b}^{(k-1)}$ is a 6×1 vector of each of the scalar accelerometer and gyro bias error estimates. Note that when $k = 1$, all six bias error estimates are initialized as zero.

The CAI-aided INS simulation mechanization equation for the CAI-measurement portion of each duty cycle k is as follows:

$$\delta \mathbf{x}_{m_{i+1}} = \mathbf{M}_d \delta \mathbf{x}_{m_i} + \mathbf{\Gamma}_d \widehat{\mathbf{u}_i}, \quad i = N - n, \dots, N \quad (3.24)$$

where $\widehat{\mathbf{u}_i}$ is a 6×1 vector of the estimated scalar accelerometer and gyro measurements provided from $\widehat{\mathbf{\Theta}}$ in the linear regression expressed in (3.9).

3.6 Revision of Model 1

Vanderbruggen and Mitchell [18] have recently proposed a numerical method to generate a collimated, continuous source of pin-polarized atoms which could be used for cold atom interferometry. Increasing the rate of available atoms should likewise increase the measurement availability. With this concept in mind, the initial integration model is revised to investigate what improvements, if any, would be gained from increasing the CAI measurement rate while maintaining the 50 percent duty cycle. CAI measurements were simulated twice per second and reflected the average of the acceleration and angular rate measurements during the two measurement duty cycles, as illustrated in Figure 3.2. Finally, the model is revised once more to simulate a 5 Hz CAI measurement rate with 50 percent duty cycle. All model results are collected and tabulated in Chapter 4.

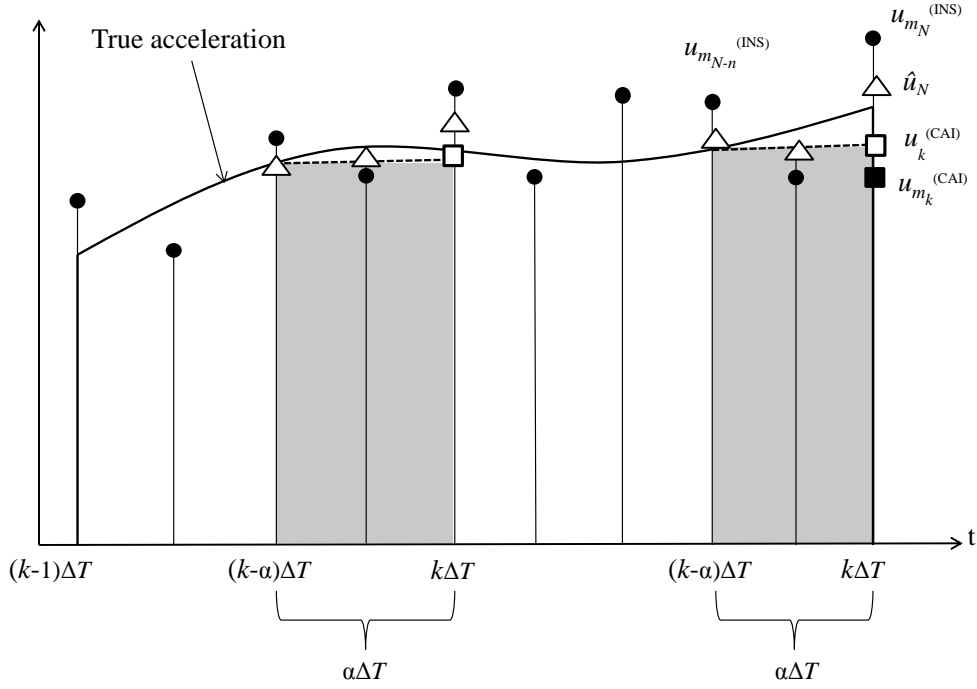


Figure 3.2: Revised Model 1. Acceleration over two CAI duty cycles.

3.7 Alternate Model

An alternate model is considered in an attempt to improve the CAI-aiding performance inspired from research conducted by Omer et al [9]. As discussed in Section I, Omer, Georgy and Noreldin integrate position and velocity measurements provided from multiple MEMs INS. The MEMs devices calculate ownship position and velocity by integrating their unique acceleration measurements. The alternate model assumes that the CAI system operates as an inertial measurement unit with its processor for calculating position, velocity and angular rate states, $\mathbf{x}^{(CAI)}$. Likewise, the conventional INS unit has its own integration processor which outputs position, velocity and angular rate states $\mathbf{x}^{(INS)}$. The conventional INS and CAI IMU state measurements are optimally combined using basic Kalman gain

principles (discussed in Chapter 2) to calculate the best estimate position, velocity, and angular rate states $\hat{\mathbf{x}}$. The best estimate $\hat{\mathbf{x}}$ is then substituted for the previously calculated $\mathbf{x}^{(\text{INS})}$ in the conventional INS mechanization equations, as shown in Figure 3.3.

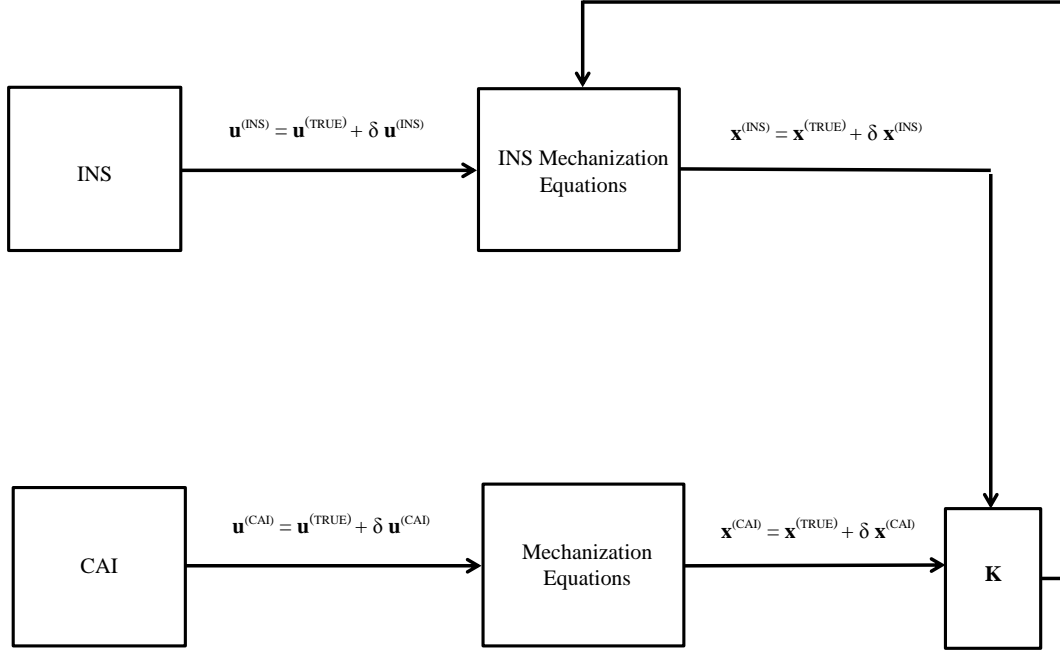


Figure 3.3: Model 2 System Concept.

The 9×1 INS and CAI state measurement vectors are defined as follows:

$$\mathbf{x}^{(\text{INS})} = \mathbf{x}^{(\text{TRUE})} + \boldsymbol{\zeta}$$

$$\mathbf{x}^{(\text{CAI})} = \mathbf{x}^{(\text{TRUE})} + \boldsymbol{\nu}$$

where $\mathbf{x}^{(\text{TRUE})}$ is the true measurement state vector, and the INS and CAI measurement error vectors are $\boldsymbol{\zeta}$ and $\boldsymbol{\nu}$, respectively. The errors are assumed to be zero-mean, stochastic variables with covariances \mathbf{P} , as expressed with the following equations:

$$\boldsymbol{\zeta} \sim \mathcal{N}(0, \mathbf{P}^{(\text{INS})})$$

$$\boldsymbol{\nu} \sim \mathcal{N}(0, \mathbf{P}^{(\text{CAI})})$$

The INS and CAI state measurement vectors may be augmented as \mathbf{z} as follows:

$$\begin{aligned} \mathbf{z} &= \mathbf{H}\mathbf{x} + \mathbf{v} \\ &= \begin{bmatrix} \mathbf{x}^{(\text{INS})} \\ \mathbf{x}^{(\text{CAI})} \end{bmatrix}_{18 \times 1} \end{aligned}$$

with regressor matrix \mathbf{H} and augmented error vector \mathbf{v}

$$\mathbf{H} = \begin{bmatrix} \mathbf{I}_{9 \times 9} \\ \mathbf{I}_{9 \times 9} \end{bmatrix}, \quad \mathbf{v} = \begin{bmatrix} \boldsymbol{\zeta} \\ \boldsymbol{\nu} \end{bmatrix}$$

and augmented covariance matrix \mathbf{R}

$$\mathbf{R} = \begin{bmatrix} \mathbf{P}^{(\text{INS})} & \mathbf{0}_{9 \times 9} \\ \mathbf{0}_{9 \times 9} & \mathbf{P}^{(\text{CAI})} \end{bmatrix}_{18 \times 18}$$

From the Kalman filter optimization discussed in Chapter 2, the estimated state vector is calculated from the following:

$$\begin{aligned} \hat{\mathbf{x}} &= \left[\mathbf{H}^{-1} \mathbf{R} \mathbf{H} \right]^{-1} \mathbf{H} \mathbf{z} \\ &= \mathbf{x}^{(\text{INS})} + \mathbf{K} \left(\mathbf{x}^{(\text{CAI})} - \mathbf{H} \mathbf{x}^{(\text{INS})} \right) \end{aligned}$$

where \mathbf{K} is the gain, defined as:

$$\mathbf{K} = \frac{\mathbf{P}^{(\text{INS})} \mathbf{H}^T}{\mathbf{H} \mathbf{P}^{(\text{INS})} \mathbf{H} + \mathbf{P}^{(\text{CAI})}}$$

This concept model would work if the CAI measurements were consistently available. However, if there were CAI accelerometer or gyro measurement dropouts due to high

dynamics, the model is no longer useful because the CAI mechanization equations would have to be re-initialized. For this reason, this alternate model was not pursued beyond a conceptual design.

IV. Results and Analysis

4.1 Monte Carlo Analysis

A Monte Carlo (MC) simulation of 1000 runs is performed to validate the navigation algorithm's performance over one hour. The aircraft's position and velocity are initialized at 0 meters and 0 (m/s), respectively. The calibrated variances of the measurement uncertainties are given in Table 4.1.

Table 4.1: Sensor Uncertainties for Scenario 1 = 1000 (m/hr), Scenario 2 = 1500 (m/hr)

Scenario 1	Bias Variance	Measurement Noise Variance
INS accelerometer	$(7.72 \times 10^{-5} \text{ m/s}^2)^2$	$(1.27 \times 10^{-2} \text{ m/s}^2 / \sqrt{\text{Hz}})^2$
INS gyro	$(6.55 \times 10^{-9} \text{ rad/hr})^2$	$(9.27 \times 10^{-7} \text{ rad} / \sqrt{\text{hr}})^2$
CAI accelerometer	N/A	$(2.00 \times 10^{-5} \text{ m/s}^2 / \sqrt{\text{Hz}})^2$
CAI gyro	N/A	$(1.47 \times 10^{-9} \text{ rad} / \sqrt{\text{hr}})^2$
Scenario 2		
INS accelerometer	$(1.16 \times 10^{-4} \text{ m/s}^2)^2$	$(1.90 \times 10^{-2} \text{ m/s}^2 / \sqrt{\text{Hz}})^2$
INS gyro	$(9.83 \times 10^{-9} \text{ rad/hr})^2$	$(1.39 \times 10^{-6} \text{ rad} / \sqrt{\text{hr}})^2$
CAI accelerometer	N/A	$(2.00 \times 10^{-5} \text{ m/s}^2 / \sqrt{\text{Hz}})^2$
CAI gyro	N/A	$(1.47 \times 10^{-9} \text{ rad} / \sqrt{\text{hr}})^2$

From this analysis, it is determined that aiding a conventional INS with CAI-based acceleration measurements, or vice versa, aiding a CAI-based INS with conventional INS measurements, reduced the navigation error by approximately 48.5 percent, as illustrated in Figure 4.1. An additional Monte Carlo simulation is run with the conventional INS position accuracy calibrated to 1500 (m/hr), reflecting navigation-grade INS specifications,

to see if the CAI aiding would be as effective. As shown in Figure 4.2, the standard deviation is reduced by approximately 47.2 percent, which suggests that the unaided system performance does not significantly impact the CAI-aiding capabilities when used with the proposed mechanization algorithm. Table 4.2 shows the unaided, aided, and percent correction for the position, velocity, and attitude parameters in both scenarios.

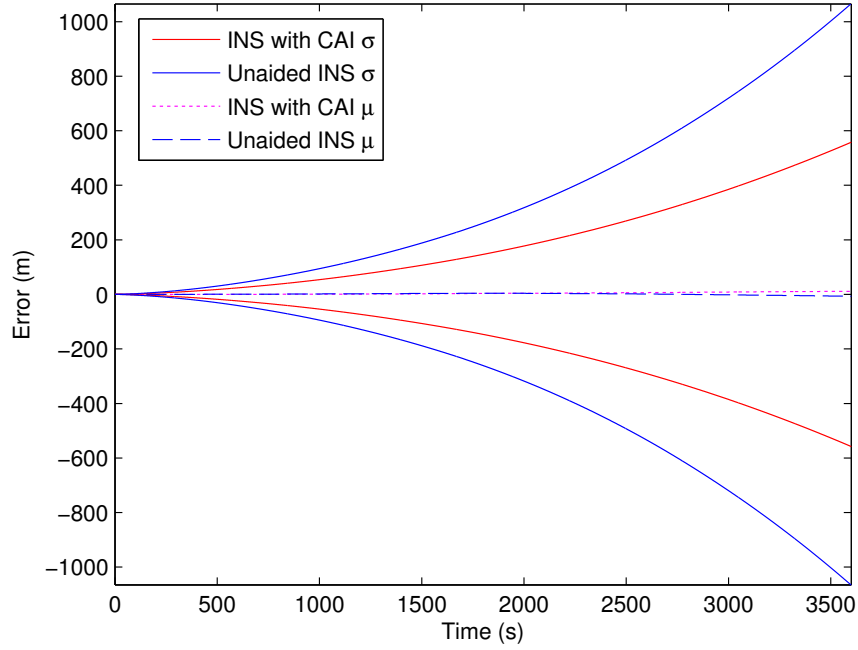


Figure 4.1: Monte Carlo Simulation results for Position Error over 1000 runs. Calibrated standard deviation position error for conventional INS is 1000 (m/hr).

4.1.1 Varying Conventional INS Data Rate.

The original simulation assumes that the CAI measurements would be aiding a conventional INS with 10 Hz data rate. This assumption is made to simplify the algorithm development; however, conventional INS systems operate at much higher data rates in the field, typically in the range of 50 to 300 Hz. To account for this disparity, the CAI-

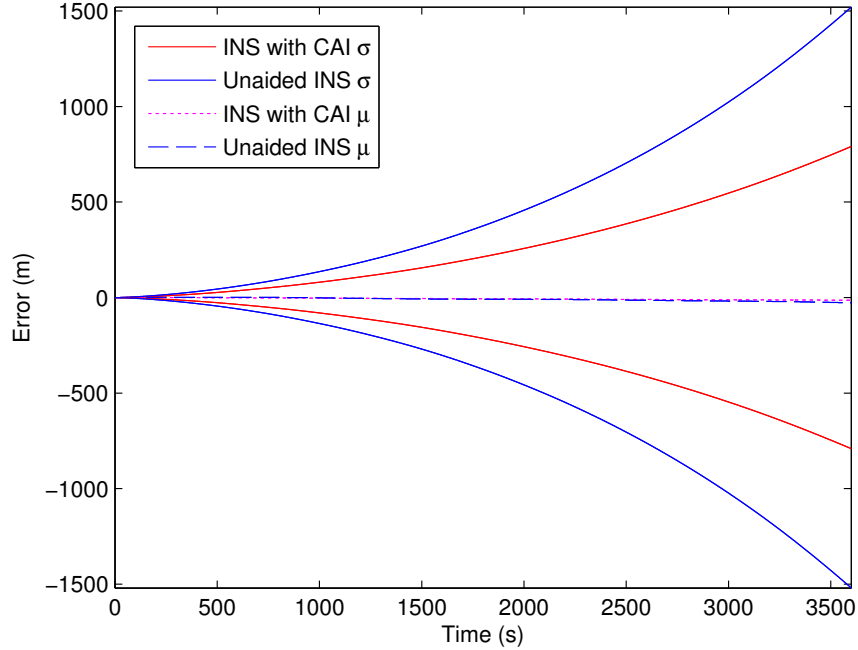


Figure 4.2: Monte Carlo Simulation results for Position Error over 1000 runs. Calibrated standard deviation position error for conventional INS was 1500 (m/hr)

aiding algorithm is tested with conventional INS sampling rates of 50 Hz, 100 Hz and 150 Hz. Computer memory limitations prevented simulations above 150 Hz. The INS drift and bias uncertainties are re-calibrated for 1500 (m/hr) drift to compensate for each of the differing data rates as shown in Table 4.3. Note that the CAI measurement data rate is kept at 1 Hz, so no recalibration was necessary. The unaided and aided RMS values for the position, velocity and attitude are given in Table 4.4. The original 10 Hz results are also included for comparison purposes. Figure 4.3 illustrates an inverse relationship between the error correction percentages and conventional INS data rates. As the data rates increase, the INS measurements are weighted more heavily and overshadow the single CAI measurement. With more samples, there is more potential for anomolous noise to enter the INS measurements which may not be accounted for by the algorithm's weighting matrix \mathbf{R} .

Table 4.2: Unaided, Aided Error and Error Correction Values after One Hour for Varied INS Drifts

1000 (m/hr) INS drift	Position (m)	Velocity (m/s)	Attitude (rad)
Unaided INS (RMS)	1051.25	0.68	2.98×10^{-5}
CAI-Aided INS (RMS)	541.85	0.34	1.40×10^{-5}
Error Correction	48.46 %	50.19 %	53.19 %
1500 (m/hr) INS drift			
Unaided INS (RMS)	1554.50	1.00	4.60×10^{-5}
CAI-Aided INS (RMS)	819.60	0.50	2.22×10^{-5}
Error Correction	47.23 %	50.18 %	51.70 %

However, the drop in aiding performance is marginal; with a fifteen-fold increase in data rate, the error correction percentage decreases by approximately six percent.

Table 4.3: Calibrated Conventional INS Uncertainties for Different Data Rates

50 Hz	Bias Variance	Measurement Noise Variance
INS accelerometer	$(1.16 \times 10^{-4} \text{ m/s}^2)^2$	$(4.25 \times 10^{-2} \text{ m/s}^2 / \sqrt{\text{Hz}})^2$
INS gyro	$(9.83 \times 10^{-9} \text{ rad/hr})^2$	$(3.11 \times 10^{-6} \text{ rad} / \sqrt{\text{hr}})^2$
100 Hz		
INS accelerometer	$(1.16 \times 10^{-4} \text{ m/s}^2)^2$	$(6.01 \times 10^{-2} \text{ m/s}^2 / \sqrt{\text{Hz}})^2$
INS gyro	$(9.83 \times 10^{-9} \text{ rad/hr})^2$	$(4.39 \times 10^{-6} \text{ rad} / \sqrt{\text{hr}})^2$
150 Hz		
INS accelerometer	$(1.16 \times 10^{-4} \text{ m/s}^2)^2$	$(7.37 \times 10^{-2} \text{ m/s}^2 / \sqrt{\text{Hz}})^2$
INS gyro	$(9.83 \times 10^{-9} \text{ rad/hr})^2$	$(5.39 \times 10^{-6} \text{ rad} / \sqrt{\text{hr}})^2$

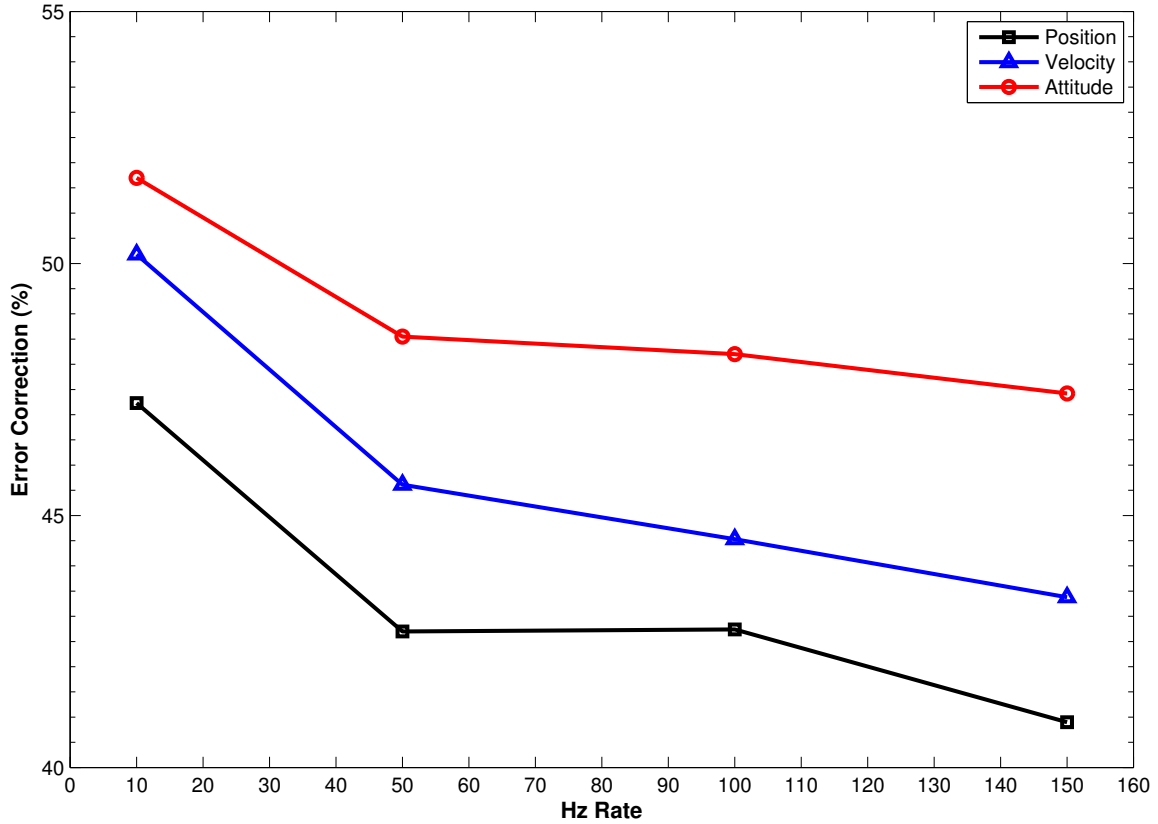


Figure 4.3: Position Error Corrections from Monte Carlo Simulations for Varying Conventional INS Data Rates.

4.1.2 Varying Acceleration Input.

In the field, the CAI-aided INS will be subjected to varying accelerations. To test its performance, two scenarios are simulated where the accelerations are 0.5 Hz sinusoidal inputs. The first acceleration waves are given an amplitude of 1.5 g's and the second, 3 g's. The 3 g amplitude represents the maximum cut-off for low dynamics, based upon the author's field test experience and previous research from Canciani [12]. CAI measurements are flagged as unusable when subjected to accelerations above 3 g's because the vibrations saturate the sensitive instruments of the low-bandwidth system. It should be noted that flagging an aiding system's measurements in poor environmental conditions, e.g. poor

Table 4.4: Unaided and Aided RMS Error after One Hour for Varied INS Data Rates

10 Hz	Position (m)	Velocity (m/s)	Attitude (rad)
Unaided INS (RMS)	1554.50	1.00	4.60×10^{-5}
CAI-Aided INS (RMS)	819.60	0.50	2.22×10^{-5}
Error Correction	47.23 %	50.18 %	51.70 %
50 Hz			
Unaided INS (RMS)	1529.13	1.02	4.30×10^{-5}
CAI-Aided INS (RMS)	876.21	0.56	2.21×10^{-5}
Error Correction	42.70 %	45.61 %	48.55 %
100 Hz			
Unaided INS (RMS)	1566.95	1.03	4.52×10^{-5}
CAI-Aided INS (RMS)	897.16	0.57	2.34×10^{-5}
Error Correction	42.74 %	44.53 %	48.20 %
150 Hz			
Unaided INS	1505.09	0.99	4.46×10^{-5}
CAI-Aided INS	889.55	0.56	2.35×10^{-5}
Error Correction	40.90 %	43.38 %	47.42 %

GPS GDOP, is a common practice in industry. For each scenario, the INS and CAI drift and bias uncertainties are re-calibrated for 1500 (m/hr) and 5 (m/hr) respectively, because the values in the transition matrix changed for different acceleration inputs. The CAI data rate are limited to 1 Hz while the INS data rates are limited to 10 Hz. The unaided, aided, and error correction values for the position, velocity and attitude are given in Table 4.5. Comparing the two scenarios, the CAI-aided INS has slightly more accurate performance when the acceleration amplitude is increased to 3 g's. This is possibly due to the CAI-aiding

being more effective when larger conventional INS errors are introduced from increased dynamics. The growth of INS errors is highly dependent upon the vehicle trajectory, as seen in the time-dependent transition matrix **A**. More scenarios should be tested before making conclusions regarding the acceleration impacts. It should also be emphasized that this trend would likely not hold in accelerations greater than 3 g's. Multiple error sources are not modeled in this research that would become more influential in high dynamics, e.g. accelerometer and gyroscope scale factors. Additionally, current CAI technology limits its measurement bandwidth to dynamics to less than 3 g's.

Table 4.5: Unaided, Aided Error and Error Correction Values after One Hour for Varied Acceleration

1.5 g Acceleration	Position (m)	Velocity (m/s)	Attitude (rad)
Unaided INS (RMS)	1579.15	1.04	4.76×10^{-5}
CAI-Aided INS (RMS)	832.08	0.52	2.22×10^{-5}
Error Correction	47.31 %	49.62 %	53.53 %
3 g Acceleration			
Unaided INS (RMS)	1623.58	1.07	4.62×10^{-5}
CAI-Aided INS (RMS)	826.07	0.52	2.16×10^{-5}
Error Correction	49.12 %	51.06 %	53.15 %

4.1.3 Varying CAI Measurement Data Rate.

As discussed in Chapter 3, recent research advances in cold atom physics have shown the potential for having continuously sourced atoms, which would allow for higher sample rates and bandwidth [18]. To test the impact of increased CAI sample rates, Monte Carlo simulations are run with 2 Hz and 5 Hz CAI data rates. The conventional INS sample rates are maintained at 10 Hz. The unaided, aided, and error correction values

for the position, velocity and attitude are given in Table 4.6, with the 1 Hz CAI data rate results included for comparison purposes. A five-fold increase in CAI data rates gave remarkable improvements in navigation accuracy, including a nearly 87 percent correction of RMS position drift error. These results demonstrate how improvements in CAI measurement availability would significantly increase the effectiveness of CAI-based aiding when implementing the proposed mechanization algorithm.

Table 4.6: Unaided, Aided Error and Error Correction Values after One Hour for Varied CAI Data Rates

1 Hz CAI	Position (m)	Velocity (m/s)	Attitude (rad)
Unaided INS (RMS)	1554.50	1.00	4.60×10^{-5}
CAI-Aided INS (RMS)	819.60	0.50	2.22×10^{-5}
Error Correction	47.23 %	50.18 %	51.70 %
2 Hz CAI			
Unaided INS (RMS)	1577.96	1.04	4.75×10^{-5}
CAI-Aided INS (RMS)	836.52	0.53	2.24×10^{-5}
Error Correction	49.99 %	49.05 %	52.91 %
5 Hz CAI			
Unaided INS (RMS)	1533.84	1.00	4.34×10^{-5}
CAI-Aided INS (RMS)	206.57	0.22	1.35×10^{-5}
Error Correction	86.53 %	77.76 %	68.96 %

V. Conclusions and Recommendations

5.1 Conclusion

High accuracy cold atom interferometers offer a potential quantum leap in inertial navigation accuracy and possibly an autonomous navigation alternative for GPS navigation. However, the CAI accelerometers and gyros' low duty cycle significantly reduces its viability as a standalone INS. Fusing the CAI-based accelerometer and gyroscope measurements together with conventional, navigation grade INS measurements increases the overall system's bandwidth while also reducing the navigation error. It should be noted that the covariance calculations add processing delay, with a minor reduction in duty cycle (dependent upon the processor capabilities). In this research, a 10 Hz free-INS's position errors are reduced by 47.2 percent by employing CAI measurements, despite the one second gaps in their availability. When the conventional INS data rate is increased to 150 Hz, the CAI-aided INS showed a marginal decrease in navigation accuracy. Increasing the CAI measurement sampling rate made a significant improvement in the CAI-aided INS performance.

5.2 Recommendations for Future Research

Further investigations should be made to determine the CAI-aiding performance during dynamic flight scenarios where the CAI may incur longer gaps between measurements, similar to research conducted by Canciani and Raquet [11].

As explained Section 1.4, the acceleration and gyro measurement models are simplified to include a single bias and drift induced error. The Earth is also assumed to be flat and non-rotating for the navigation simulations. More complex error and mechanics models are proposed in [11] and [19]. These models could be employed to make a realistic evaluation of their contributive effects in more dynamic flight scenarios.

Errors caused from the processing delay or lag should be investigated in a real-time model. The errors caused from gaps in acceleration and angular rate measurements become more significant when those corresponding dynamics are rapidly changing, particularly in medium to high dynamics. The developed algorithm performance could be compared with an extended Kalman filter which estimate the INS mechanization during gaps in CAI-aiding. Increased CAI measurement availability may reduce the impact from these delays.

Cold atom technology is developing at a fast pace due to its application in multiple areas where precision measurements are a necessity. As more CAI improvements and demonstrations are made, system limitations and parameters should be updated to reflect actual performance. Ideally, flight testing of actual CAI hardware could be performed in the future to test advanced mechanization models and their aiding algorithms.

Appendix A: Analytic Sensor Drift Modeling

A.1 Gyro Drift

The continuous-time rate gyro dynamics are modeled as a stochastic differential equation

$$\dot{\theta}(t) = \omega(t) + b_G + \sigma_{\theta_c} \dot{\beta}(t), \quad \theta(0) = 0 \quad (\text{A.1})$$

where $\omega(t)$ is the true input angular rate, b_G is the gyro's residual random bias $b_G \sim \mathcal{N}(0, \sigma_{b_G}^2)$ and the stochastic process $\beta(\cdot)$ is a unit Brownian motion, that is, $\beta(t) \sim \mathcal{N}(0, t)$. Note that the units of the strength of the gyro's drift parameter σ_{θ_c} are (rad/ \sqrt{s}). If $\omega(t) \equiv 0$ and $b_G \equiv 0$, the solution to the stochastic differential equation (A.1) is as follows:

$$\theta(t) \sim \mathcal{N}(0, \sigma_{\theta_c}^2 t) \quad (\text{A.2})$$

The specified rate gyro's measurement uncertainty caused by drift σ_θ is defined as the angular position uncertainty brought about by integrating the rate gyro's output over one hour. In industry, it is commonly referred to as the Angle Random Walk (ARW) specification because the gyro drift introduces a zero-mean random walk error in the angle [10]. In other words, if the true angular rate $\omega(t) \equiv 0$, then at one hour, the following is true:

$$\theta(3600) \sim \mathcal{N}(0, \sigma_\theta^2) \quad (\text{A.3})$$

Relating equations (A.2) and (A.3) when $t = 3600$, and using the manufacturer's provided gyro specification σ_θ , we obtain

$$\sigma_{\theta_c} = \frac{\sigma_\theta}{60 \cdot \frac{180}{\pi}} \quad (\text{rad}/\sqrt{s}) \quad (\text{A.4})$$

which defines the parameter σ_{θ_c} featured in the continuous-time gyro dynamics modeled by the stochastic differential equation in (A.1) and in the continuous-time INS navigation state error equation in (3.17).

The discrete-time form of (A.1) is as follows:

$$\theta_{i+1} = \theta_i + (\omega_i + b_G)\Delta T + \sigma_{\theta_d}\eta_i, \quad \theta_0 = 0, \quad i = 0, 1, \dots \quad (\text{A.5})$$

where the intensity of the process noise, σ_{θ_d} , is the discrete-time equivalent of the parameter σ_{θ_c} . The random variable η_i is stipulated as $\eta_i \sim \mathcal{N}(0, 1)$. When $\omega_i \equiv 0$ and $b_G \equiv 0$, the solution to the discrete-time stochastic difference equation (A.5) is:

$$\begin{aligned} \theta_i &= \sigma_{\theta_d} \sum_{i=0}^{i-1} \eta_i \\ &\sim \mathcal{N}\left(0, i\sigma_{\theta_d}^2\right), \quad i = 0, 1, \dots \end{aligned} \quad (\text{A.6})$$

Since ΔT is related to the sampling rate f_s through the following equation:

$$\Delta T = \frac{1}{f_s}$$

then after one hour, $i = 3600 \cdot f_s$, where we recall the units of Hz are (1/s). From (A.3), (A.4), and (A.6), the parameter featured in the stochastic difference equation (A.5) is as follows:

$$\begin{aligned} \sigma_{\theta_d} &= \frac{\sigma_{\theta}}{60 \cdot \frac{180}{\pi}} \cdot \sqrt{\Delta T} \\ &= \frac{\sigma_{\theta_c}}{\sqrt{f_s}} \quad (\text{rad}) \end{aligned}$$

Assuming the gyro drift and gyro bias uncertainties are the only error sources, the continuous-time navigation state error equation (3.17) would be specified as follows:

$$\delta \dot{\mathbf{x}}_c(t) = \mathbf{M}_c \delta \mathbf{x}_c(t) + \mathbf{\Gamma}_{G_c} \mathbf{b}_G + \sigma_{\theta_c} \mathbf{\Gamma}_{G_c} \dot{\boldsymbol{\beta}}_G(t) \quad (\text{A.7})$$

where $\mathbf{b}_G \sim \mathcal{N}(0, \sigma_{b_G}^2 \mathbf{I})$, $\boldsymbol{\beta}_G$ is a 3×1 vector of independent unity Brownian motions, and

$$\mathbf{\Gamma}_{G_c} = \begin{bmatrix} \mathbf{0} \\ \mathbf{0} \\ \mathbf{I} \end{bmatrix}$$

Note that in (A.7) the units of σ_{b_G} are (rad/s). If σ_{b_G} is specified in terms of (deg/hr), then convert σ_{b_G} to (rad/s) using the following equation:

$$\sigma_{b_G} \text{ (rad/s)} := \sigma_{b_G} \cdot \frac{1}{3600 \cdot \frac{180}{\pi}}$$

The discrete-time form of the navigation state error equation (A.7) is

$$\delta \mathbf{x}_{i+1} = \mathbf{M}_d \delta \mathbf{x}_i + \mathbf{\Gamma}_{G_d} \mathbf{b}_{G_i} + \sigma_{\theta_d} \mathbf{\Gamma}_{G_c} \mathbf{w}_{G_i}, \quad \delta \mathbf{x}_0 = 0 \quad (\text{A.8})$$

where

$$\mathbf{\Gamma}_{G_d} = \mathbf{M}_d \cdot \left(\int_0^{\Delta T} e^{\mathbf{M}_c(-\tau)} d\tau \right) \mathbf{\Gamma}_{G_c},$$

\mathbf{w}_{G_i} is a 3×1 vector of independent, Gaussian random variables with $\mathbf{w}_{G_i} \sim \mathcal{N}(0, \mathbf{I})$ for $i = 0, 1, \dots$ and \mathbf{b}_{G_i} is a 3×1 vector of constant, random biases, that is, $\mathbf{b}_{G_{i+1}} = \mathbf{b}_{G_i}$, $\mathbf{b}_{G_0} \sim \mathcal{N}(0, \sigma_{b_G}^2 \mathbf{I})$. The constant gyro biases may be augmented into the state vector, such that (A.8) becomes

$$\delta \mathbf{x}_{i+1} = \mathbf{A}_G \delta \mathbf{x}_i + \sigma_{\theta_d} \mathbf{G}_G \mathbf{w}_{G_i} \quad (\text{A.9})$$

$$\delta \mathbf{x}_0 \sim \mathcal{N} \left(0, \begin{bmatrix} \mathbf{0} & \mathbf{0} \\ \mathbf{0} & \sigma_{b_G}^2 \mathbf{I} \end{bmatrix} \right)$$

where

$$\mathbf{A}_G = \begin{bmatrix} \mathbf{M}_d & \mathbf{\Gamma}_{G_d} \\ \mathbf{0} & \mathbf{I} \end{bmatrix}, \quad \mathbf{G}_G = \sigma_{\theta_d} \begin{bmatrix} \mathbf{\Gamma}_{G_c} \\ \mathbf{0} \end{bmatrix}$$

A.2 Accelerometer Drift

The continuous-time accelerometer dynamics are modeled as

$$\dot{v}(t) = u(t) + b_A + \sigma_{v_d} \dot{\beta}(t), \quad v(0) = 0 \quad (\text{A.10})$$

where $u(t)$ is the true acceleration, b_A is the accelerometer's random bias $b_A \sim \mathcal{N}(0, \sigma_{b_A}^2)$, and $\beta(t)$ is a unit Brownian motion. Hence, the units of σ_{v_d} are (m/s \sqrt{s}). If the true

acceleration $u(t) \equiv 0$ and $b_A \equiv 0$, the solution of the stochastic differential equation in (A.10) is as follows:

$$v(t) \sim \mathcal{N}(0, \sigma_{v_c}^2 t) \quad (\text{A.11})$$

The acceleration measurement uncertainty caused by drift σ_v (m/s) is specified as the velocity uncertainty brought about by integrating the accelerometer's output over one hour. The accelerometer drift introduces a zero-mean random walk error in the velocity output, so it is aptly called the Velocity Random Walk (VRW) specification [10]. In other words, if the true acceleration $u(t) \equiv 0$, then at one hour:

$$v(3600) \sim \mathcal{N}(0, \sigma_v^2) \quad (\text{A.12})$$

From (A.11) and (A.12), when $t = 3600$, σ_{v_c} is as follows:

$$\sigma_{v_c} = \frac{\sigma_v}{60} \quad (\text{m/s } \sqrt{\text{s}})$$

thus calculating the parameter σ_{v_c} which features in the stochastic differential equation (A.10) using the manufacturer supplied specification σ_v .

Converting the dynamics (A.10) to discrete-time form gives the following equation:

$$v_{i+1} = v_i + (u_i + b_A)\Delta T + \sigma_{v_d}\eta_i, \quad v_0 = 0 \quad (\text{A.13})$$

where σ_{v_d} is the discrete-time equivalent of σ_{v_c} and as before, $\eta_i \sim \mathcal{N}(0, 1)$. When $u_i \equiv 0$ and $b_A \equiv 0$, the following is true:

$$v_i \sim \mathcal{N}(0, i\sigma_{v_d}^2), \quad i = 0, 1, \dots \quad (\text{A.14})$$

From (A.11), (A.12), and (A.14), the parameter featured in the stochastic difference equation (A.13) is:

$$\sigma_{v_d} = \frac{\sigma_{v_c}}{\sqrt{f_s}} \quad (\text{m/s})$$

Finally, including the accelerometer bias and drift error sources in the navigation state error dynamics equation (A.7) gives the following equation:

$$\delta \dot{\mathbf{x}}_c(t) = \mathbf{M}_c \delta \mathbf{x}_c(t) + \mathbf{\Gamma}_{G_c} \mathbf{b}_G + \sigma_{\theta_c} \mathbf{\Gamma}_{G_c} \dot{\boldsymbol{\beta}}_G(t) + \mathbf{\Gamma}_{A_c} \mathbf{b}_A + \sigma_{v_c} \mathbf{\Gamma}_{A_c} \dot{\boldsymbol{\zeta}}_A(t) \quad (\text{A.15})$$

where

$$\mathbf{\Gamma}_{A_c} = \begin{bmatrix} \mathbf{0} \\ \mathbf{I} \\ \mathbf{0} \end{bmatrix}$$

$\boldsymbol{\beta}_A$ is a 3×1 vector of independent unity Brownian motions, and $\mathbf{b}_A \sim \mathcal{N}(0, \sigma_{b_A}^2 \mathbf{I})$. Note that the accelerometer bias variance, $\sigma_{b_A}^2$, is given in Table 4.1. Re-writing (A.15) in discrete-time form yields the following expression:

$$\delta \mathbf{x}_{i+1} = \mathbf{M}_d \delta \mathbf{x}_i + \mathbf{\Gamma}_{G_d} \mathbf{b}_{G_i} + \sigma_{\theta_d} \mathbf{\Gamma}_{G_c} \mathbf{w}_{G_i} + \mathbf{\Gamma}_{A_d} \mathbf{b}_{A_i} + \sigma_{v_d} \mathbf{\Gamma}_{A_c} \mathbf{w}_{A_i}, \quad \delta \mathbf{x}_0 = 0 \quad (\text{A.16})$$

where

$$\mathbf{\Gamma}_{A_d} = \mathbf{M}_d \cdot \left(\int_0^{\Delta T} e^{\mathbf{M}_c(-\tau)} d\tau \right) \mathbf{\Gamma}_{A_c}$$

\mathbf{w}_{A_i} is a 3×1 vector of independent, Gaussian random variables: $\mathbf{w}_{A_i} \sim \mathcal{N}(0, \mathbf{I})$ and \mathbf{b}_{A_i} is a 3×1 vector of constant, random biases: $\mathbf{b}_{A_{i+1}} = \mathbf{b}_{A_i}$, $\mathbf{b}_{A_0} \sim \mathcal{N}(0, \sigma_{b_A}^2 \mathbf{I})$.

The accelerometer and gyro biases may be augmented into the navigation state vector as follows:

$$\delta \mathbf{x}_i = \begin{bmatrix} \delta \mathbf{x}_i \\ \mathbf{b}_{A_i} \\ \mathbf{b}_{G_i} \end{bmatrix}$$

such that in the absence of alignment errors, the discrete-time navigation state error dynamics equation in (A.16) becomes

$$\delta \mathbf{x}_{i+1} = \mathbf{A} \delta \mathbf{x}_i + \mathbf{G} \sqrt{\mathbf{Q}} \mathbf{w}_i, \quad \delta \mathbf{x}_0 \sim \mathcal{N} \left(0, \begin{bmatrix} \mathbf{0}_{9 \times 9} & \mathbf{0} & \mathbf{0} \\ \mathbf{0}_{3 \times 9} & \sigma_{b_A}^2 \mathbf{I} & \mathbf{0} \\ \mathbf{0}_{3 \times 9} & \mathbf{0} & \sigma_{b_G}^2 \mathbf{I} \end{bmatrix} \right) \quad (\text{A.17})$$

where

$$\mathbf{A} = \begin{bmatrix} \mathbf{M}_d & \mathbf{\Gamma}_{A_d} & \mathbf{\Gamma}_{G_d} \\ \mathbf{0} & \mathbf{I} & \mathbf{0} \\ \mathbf{0} & \mathbf{0} & \mathbf{I} \end{bmatrix}_{15 \times 15}, \quad \mathbf{G} = \begin{bmatrix} \mathbf{\Gamma}_{A_c} & \mathbf{\Gamma}_{G_c} \\ \mathbf{0}_{6 \times 3} & \mathbf{0}_{6 \times 3} \end{bmatrix}_{15 \times 6}$$

$$\mathbf{Q} = \begin{bmatrix} \sigma_{v_d}^2 \mathbf{I} & \mathbf{0} \\ \mathbf{0} & \sigma_{\theta_d}^2 \mathbf{I} \end{bmatrix}_{6 \times 6}, \quad \mathbf{w}_i = \begin{bmatrix} \mathbf{w}_{A_i} \\ \mathbf{w}_{G_i} \end{bmatrix}_{6 \times 1}$$

Appendix B: Calibration for Bias and Drift Uncertainty

In the conventional INS and in the CAI-based Inertial Measurement Unit (IMU), the accelerometer and gyroscope measurement errors at discrete time $i = 1, 2, \dots$, caused by drift are white, Gaussian noises $w_{A_i} \sim \mathcal{N}(0, 1)$ and $w_{G_i} \sim \mathcal{N}(0, 1)$, respectively [15]. Similarly, the accelerometer and gyroscopes' unknown, but constant, bias errors are $b_A \sim \mathcal{N}(0, \sigma_{b_A}^2 \mathbf{I})$ and $b_G \sim \mathcal{N}(0, \sigma_{b_G}^2 \mathbf{I})$. The biases \mathbf{b}_A and \mathbf{b}_G are 3×1 vectors and their uncertainties are quantified by the accelerometer and gyroscope specifications, $\sigma_{b_A}^2$ and $\sigma_{b_G}^2$, respectively.

We determine σ_{v_d} , σ_{θ_d} , σ_{b_A} and σ_{b_G} by calibration, so that the conventional, navigation grade INS yields a positional error of 1 (km/ $\sqrt{\text{hr}}$) and the CAI-based IMU in theory yields a position error of 5 (m/ $\sqrt{\text{hr}}$). This entails a covariance analysis.

The covariance of the navigation state's error satisfies the Lyapunov equation as follows [13]:

$$\mathbf{P}_{i+1}^{(\delta x)} = \mathbf{A} \mathbf{P}_i^{(\delta x)} \mathbf{A}^T + \mathbf{G} \mathbf{Q} \mathbf{G}^T, \quad i = 0, 1, \dots, N-1 \quad (\text{B.1})$$

where \mathbf{Q} is the accelerometers' and gyroscopes' drift uncertainties matrix

$$\mathbf{Q} = \begin{bmatrix} \sigma_{v_d}^2 \mathbf{I} & \mathbf{0} \\ \mathbf{0} & \sigma_{\theta_d}^2 \mathbf{I} \end{bmatrix}$$

and N is such that one hour is considered. Assuming no alignment errors, the covariance matrix is initialized as follows:

$$\mathbf{P}_0^{(\delta X)} = \begin{bmatrix} \mathbf{0}_{9 \times 9} & \mathbf{0}_{9 \times 3} & \mathbf{0}_{9 \times 3} \\ \mathbf{0}_{3 \times 9} & \sigma_{b_A}^2 \mathbf{I} & \mathbf{0}_{3 \times 3} \\ \mathbf{0}_{3 \times 9} & \mathbf{0}_{3 \times 3} & \sigma_{b_G}^2 \mathbf{I} \end{bmatrix}$$

and it is required that the x position uncertainty of the conventional INS after one hour be specified as follows:

$$\sqrt{\left(\mathbf{P}_{3600-N}^{(\delta X)}\right)_{1,1}} = 1000 \quad \text{m}$$

Note that there is a linear relationship between the sensors' drift induced measurement error variances, $\sigma_{v_d}^2$ and $\sigma_{\theta_d}^2$; the variance $\sigma_{b_A}^2$ and $\sigma_{b_G}^2$ of sensor biases; and the uncertainty in the aircraft final x position:

$$\left(\mathbf{P}_{3600 \cdot N}^{(\delta X)}\right)_{1,1} = \alpha \sigma_{v_d}^2 + \beta \sigma_{\theta_d}^2 + \alpha_b \sigma_{b_A}^2 + \beta_b \sigma_{b_G}^2$$

The coefficients α , β , α_b , and β_b are determined by sequentially setting all but one uncertainty to zero in a sequential manner and solving equation (B.1) four times as follows:

$$\begin{aligned}\alpha &= \left(\mathbf{P}_{3600 \cdot N}^{(\delta X)}\right)_{1,1}, \quad \sigma_{v_d} = 1, \sigma_{\theta_d} = 0, \sigma_{b_A} = 0, \sigma_{b_G} = 0 \\ \beta &= \left(\mathbf{P}_{3600 \cdot N}^{(\delta X)}\right)_{1,1}, \quad \sigma_{v_d} = 0, \sigma_{\theta_d} = 1, \sigma_{b_A} = 0, \sigma_{b_G} = 0 \\ \alpha_b &= \left(\mathbf{P}_{3600 \cdot N}^{(\delta X)}\right)_{1,1}, \quad \sigma_{v_d} = 0, \sigma_{\theta_d} = 0, \sigma_{b_A} = 1, \sigma_{b_G} = 0 \\ \beta_b &= \left(\mathbf{P}_{3600 \cdot N}^{(\delta X)}\right)_{1,1}, \quad \sigma_{v_d} = 0, \sigma_{\theta_d} = 0, \sigma_{b_A} = 0, \sigma_{b_G} = 1\end{aligned}$$

The uncertainty standard deviations are then determined from the following equations:

$$\begin{aligned}\sigma_{v_d} &= \sqrt{\frac{\left(\mathbf{P}_{3600 \cdot N}^{(\delta X)}\right)_{1,1}}{2\alpha}}, & \sigma_{\theta_d} &= \sqrt{\frac{\left(\mathbf{P}_{3600 \cdot N}^{(\delta X)}\right)_{1,1}}{2\beta}} \\ \sigma_{b_A} &= \sqrt{\frac{\left(\mathbf{P}_{3600 \cdot N}^{(\delta X)}\right)_{1,1}}{2\alpha_b}}, & \sigma_{b_G} &= \sqrt{\frac{\left(\mathbf{P}_{3600 \cdot N}^{(\delta X)}\right)_{1,1}}{2\beta_b}}\end{aligned}$$

where $\left(\mathbf{P}_{3600 \cdot N}^{(\delta X)}\right)_{1,1}$ is the required x position variance after a one hour flight.

For the conventional free INS, where $\delta t = 0.1$ seconds ($N = 10$), we require $\left(\mathbf{P}_{3600 \cdot N}^{(\delta X)}\right)_{1,1} = 10^6$ (m²), such that after one hour the x -axis position uncertainty standard deviation is 1 (km). The calculated measurement variances, $\sigma_{v_d}^2$ and $\sigma_{\theta_d}^2$, which account for the acceleration and gyro drifts and the residual bias uncertainties $\sigma_{b_A}^2$ and $\sigma_{b_G}^2$, are given in Table 4.1 for both the INS and CAI IMUs.

The CAI IMU's discrete-time navigation state error covariance equations are the same as (B.1), with the required $\left(\mathbf{P}_{3600 \cdot N}^{(\delta X)}\right)_{1,1} = 25$ (m²) such that after one hour the theoretical position uncertainty standard deviation is 5 (m).

Bibliography

- [1] A. C. [Photograph]. Accessed from: physweb.bgu.ac.il, Jan. 2014.
- [2] R. G. Brown and P. Y. C. Hwang, *Introduction to Random Signals and Applied Kalman Filtering*. New York, NY: J. Wiley, 1996.
- [3] P. S. Maybeck, *Stochastic Models, Estimation, and Control: Volume 1*. New York, NY: Academic Press Inc., 1979.
- [4] W. F. Storms, "Magnetic field aided indoor navigation," Master's thesis, Air Force Institute of Technology, Wright Patterson AFB, OH, 2009.
- [5] J. Wang and et al, "Cold atom interferometers and their applications in precision measurements," *Frontiers of Physics in China*, vol. 4, no. 2, 2009.
- [6] J. Fang and J. Qin, "Advances in atomic gyroscopes: A view from inertial navigation applications," *Sensors*, vol. 12, no. 1424, 2012.
- [7] V. Leung and et al, "Magnetic-film atom chip setup with 10 μm period lattices of magnetic microtraps," *eprint arXiv*, vol. 1311, 2013.
- [8] C. Jekeli, "Navigation error analysis of atom interferometer inertial sensor," *Navigation: Journal of the Institute of Navigation*, vol. 52, no. 1, 2005.
- [9] M. B. Nielsen, "Development and flight test of a robust optical-inertial navigation system using low-cost sensors," Master's thesis, Air Force Institute of Technology, Wright Patterson AFB, OH, 2008.
- [10] M. de Angelis and et al, "Precision gravimetry with atomic sensors," *Measurement Science and Technology*, vol. 20, no. 2, 2009.
- [11] A. N. Medhat Omer, Jacques Georgy, "Using multiple sensor triads for enhancing the navigation solution of portable and wearable devices," in *Proceedings of the 2013 International Technical Meeting of the Institute of Navigation*, (Nashville, TN), ION, 2013.
- [12] O. J. Woodman, "An introduction to inertial navigation," UCAM-CL-TR-696, University of Cambridge, Aug. 2007.
- [13] A. Canciani and J. Raquet, "Integration of cold atom interferometry ins with other sensors," in *Proceedings of the 2012 International Technical Meeting of the Institute of Navigation*, (Newport Beach, CA), pp. 151–185, ION, 2012.
- [14] A. Canciani, "Integration of cold atom interferometry ins with other sensors," Master's thesis, Air Force Institute of Technology, Wright Patterson AFB, OH, 2007.

- [15] M. Pachter. Course Handouts, EENG 635, Inertial Navigation Subsystems, Feb. 2013.
- [16] K. Fisher. Course Handouts, EENG 766, Stochastic Modeling Estimation and Control II, Feb. 2013.
- [17] J. Quarmyne, “Inertial navigation system aiding using vision,” Master’s thesis, Air Force Institute of Technology, Wright Patterson AFB, OH, 2013.
- [18] T. Vanderbruggen and M. Mitchell, “Near-resonant optical forces beyond the two-level approximation for a continuous source of spin-polarized cold atoms,” *Physical Review A*, vol. 87, no. 3, 2013.
- [19] W. S. F. John H. Wall and D. M. Bevly, “Characterization of various imu error sources and the effect on navigation performance,” in *Proceedings of the 18th International Technical Meeting of the Satellite Division of The Institute of Navigation*, (Long Beach, CA), ION, 2005.

REPORT DOCUMENTATION PAGE					<i>Form Approved</i> OMB No. 0704-0188	
The public reporting burden for this collection of information is estimated to average 1 hour per response, including the time for reviewing instructions, searching existing data sources, gathering and maintaining the data needed, and completing and reviewing the collection of information. Send comments regarding this burden estimate or any other aspect of this collection of information, including suggestions for reducing this burden to Department of Defense, Washington Headquarters Services, Directorate for Information Operations and Reports (0704-0188), 1215 Jefferson Davis Highway, Suite 1204, Arlington, VA 22202-4302. Respondents should be aware that notwithstanding any other provision of law, no person shall be subject to any penalty for failing to comply with a collection of information if it does not display a currently valid OMB control number. PLEASE DO NOT RETURN YOUR FORM TO THE ABOVE ADDRESS.						
1. REPORT DATE (DD-MM-YYYY) 27-03-2014		2. REPORT TYPE Master's Thesis		3. DATES COVERED (From — To) Oct 2013–Mar 2014		
4. TITLE AND SUBTITLE Signal Processing in Cold Atom Interferometry-Based INS				5a. CONTRACT NUMBER 5b. GRANT NUMBER 5c. PROGRAM ELEMENT NUMBER		
6. AUTHOR(S) Willis, Kara M., Civilian, DAF				5d. PROJECT NUMBER JON 14G240B 5e. TASK NUMBER 5f. WORK UNIT NUMBER		
7. PERFORMING ORGANIZATION NAME(S) AND ADDRESS(ES) Air Force Institute of Technology Graduate School of Engineering and Management (AFIT/EN) 2950 Hobson Way WPAFB, OH 45433-7765				8. PERFORMING ORGANIZATION REPORT NUMBER AFIT-ENG-14-M-84		
9. SPONSORING / MONITORING AGENCY NAME(S) AND ADDRESS(ES) Air Force Research Laboratory POC: Dr. Stewart DeVilbiss, nathan.devilbiss.ctr@us.af.mil and Dr. Jacob Campbell, jacob.campbell.3@us.af.mil 2241 Avionics Circle Area B, Building 620 WPAFB, OH 45433-7321				10. SPONSOR/MONITOR'S ACRONYM(S) AFRL/RV 11. SPONSOR/MONITOR'S REPORT NUMBER(S)		
12. DISTRIBUTION / AVAILABILITY STATEMENT DISTRIBUTION STATEMENT A: APPROVED FOR PUBLIC RELEASE; DISTRIBUTION UNLIMITED						
13. SUPPLEMENTARY NOTES This work is declared a work of the U.S. Government and is not subject to copyright protection in the United States.						
14. ABSTRACT High precision Cold Atom Interferometers (CAI) are in development to supplement or replace conventional, navigation quality inertial measurement units. A major drawback of the atomic interferometers is their low duty cycle and sampling rate, caused by delays required for cooling the atoms and collecting acceleration and angular rate measurements. A method is herein developed for inertial navigation by integrating highly accurate, low duty cycle CAI measurements with high bandwidth, conventional Inertial Navigation System (INS) measurements. A fixed-lag smoothing algorithm is used to estimate optimal acceleration and angular rate measurements from the CAI and INS data. Given current CAI limitations, simulation results demonstrate nearly 50 percent error reduction for the enhanced INS compared to a conventional, unaided INS. When the conventional INS position error was increased by 500 (m/hr), the 50 percent error reduction from aiding was maintained. Increasing the conventional INS data rate fifteen-fold while maintaining a 1 Hz CAI sample rate leads to an approximately 6 percent increase in navigation error, suggesting that the CAI-aiding algorithm effectivity is only slightly influenced by the conventional INS data rates. A five-fold increase of the CAI measurement rate shows approximately 80 percent reduction in navigation error, supporting the potential for significant performance gains in the near future from advancements in cold atom technology.						
15. SUBJECT TERMS Cold Atom Interferometry, Dual INS Integration, Atomic Navigation Sensors						
16. SECURITY CLASSIFICATION OF:			17. LIMITATION OF ABSTRACT UU	18. NUMBER OF PAGES 74	19a. NAME OF RESPONSIBLE PERSON Dr. Meir Pachter (ENG)	
a. REPORT U	b. ABSTRACT U	c. THIS PAGE U			19b. TELEPHONE NUMBER (include area code) (937) 255-3636 x7247 meir.pachter@afit.edu	